

交通部中央氣象局

委託研究計畫(期中/期末)成果報告

臺灣地區 108 年中大型地震震源資訊之快速彙整與提供  
中大規模地震震源破裂特性近即時分析

計畫類別：氣象    海象    地震

計畫編號：MOTC-CWB-108-E-03

執行期間：108 年 1 月 1 日至 108 年 12 月 31 日

計畫主持人：李憲忠

執行機構：中央研究院地球科學研究所

本成果報告包括以下應繳交之附件(或附錄)：

- 赴國外出差或研習心得報告 1 份
- 赴大陸地區出差或研習心得報告 1 份
- 出席國際學術會議心得報告及發表之論文各 1 份

中華民國 108 年 11 月 18 日

## 政府研究計畫(期中/期末)報告摘要資料表

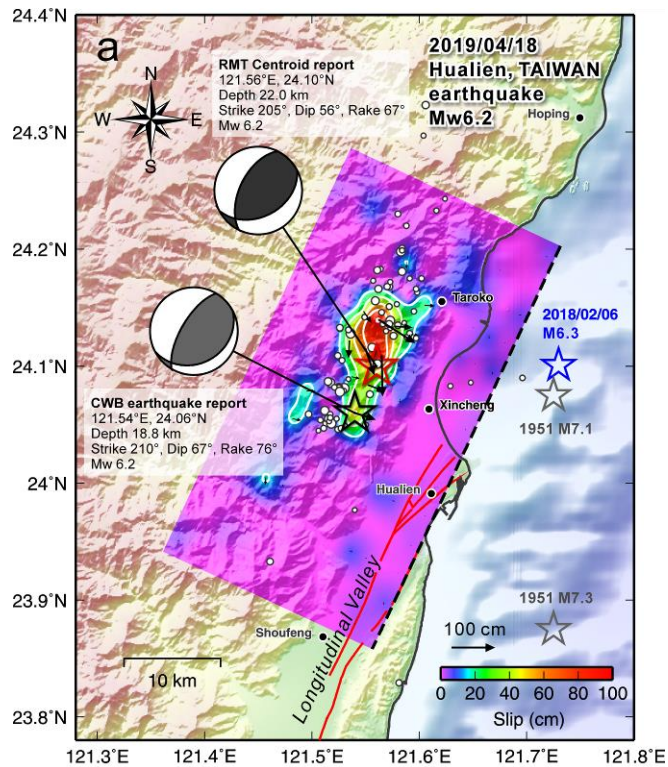
計畫中文名稱	臺灣地區 108 年中大型地震震源資訊之快速彙整與提供 - 中大規模地震震源破裂特性近即時分析		
計畫編號	MOTC-CWB-108-E-03		
主管機關	交通部中央氣象局		
執行機構	中央研究院地球科學研究所		
年度	108	執行期間	108.1.1-108.12.31
本期經費 (單位：千元)	1024.896		
執行進度	預定 (%)	實際 (%)	比較 (%)
	100	100	100
經費支用	預定(千元)	實際(千元)	支用率 (%)
研究人員	計畫主持人	協同主持人	研究助理
	李憲忠		
報告頁數	31	使用語言	中文、英文
中英文關鍵詞	2019/04/18 花蓮地震、震源破裂過程分析		
研究目的	<p>(簡述研究計畫之目的及意義，約 300 字。)</p> <p>本計畫針對台灣地區中大規模地震進行震源破裂特性近即時分析。所採用的方法為體波震源逆推法，此方法在進行分析前需要完整的震源參數資訊，包括地震規模、震源位置、震源機制、斷層面解等，目前這些資訊氣象局已經於地震發生後快速地做例行公布，因此在現有的資訊架構下，於中大型地震發生後快速建立震源破裂過程的初步結果是可以達到的。本研究將透過世界地震觀測網的遠震體波資料或中央氣象局即時強震網的近場資料，依地震規模大小以不同資料進行震源逆推。針對台灣中大型地震進行震源模式分析，可對發震區的震源破裂特性有更清楚的瞭解，同時所建立之震源破裂模型對於後續之研究，如庫倫應力轉移分析、地震波傳遞模擬與強地動評估等可提供重要的資訊。由長遠目標來看，震源破裂模型持續、有系統地分析與建立將可幫助地震與地質等基礎研究，亦可於地</p>		

震防災、減災上做出貢獻。

研究成果

(說明研究之具體成果，約 800~1000 字，並附一張圖說明。)

2019 年 4 月 18 日花蓮海域發生規模 6.1 地震 (Mw 6.2)，是今年於台灣島內第一個芮氏規模大於 6 的地震。中央氣象局地震報告指出，此地震位於花蓮縣政府西北方約 10 公里，震源深度 18.8 公里。各單位所求得之震源機制解相當一致，大致為北北東-南南西走向之斜向逆衝斷層 (圖一)。主餘震定位的結果亦呈現北北東-南南西走向分布，符合震源機制解其中的一個斷層面。雖然震央位在花蓮，但整個北台灣都出現強烈振動，最大震度出現在花蓮縣銅門，震度達到 7 級；花蓮市區達震度 5，台北亦出現震度 4 級且長時間的持續搖晃，造成市區內兩棟高樓碰撞與輕微損壞，所幸這次地震沒有造成人員傷亡。為了瞭解這個地震究竟如何發生、破裂過程為何，本研究採用近場地動資料進行震源逆推。研究中採用氣象局之震源位置，並以 RMT 震源機制解中的南北走向，朝西下傾的斷層面做為斷層模型，以平行化非負最小平方法來進行震源逆推，藉由震源破裂的時間-空間過程來研判此次地震的震源物理特性以及構造上的意義。



圖一、2019 花蓮地震錯動量分佈分析結果。

<p>具體落實應用情形</p>	<p>(說明成果之價值與貢獻、技術移轉、應用推廣等情形，約 300 字。)</p> <p>以近場地動資料震源逆推的結果指出，此地震的破裂範圍約 10 x 10 km<sup>2</sup>，最大錯動量約 101.8 cm。震源附近於發震後短時間內 0~1 秒的滑移量不大，隨後破裂以較快的破裂速度(大於 3.0 km/s)朝北發展，約在 2.5 秒時破裂傳到斷層北邊釋放大量的能量，並形成斷層面上最大的錯動集中區(Asperity)。隨後破裂快速減緩，僅產生零星的小錯動。整個破裂持續時間約 7-8 秒，一開始的 1-2 秒能量在震源附近釋放，於 2-5 秒時破裂主要發生在北邊的 Asperity，為此次地震主要的能量釋放，5 秒後的能量於北側斷層零星產生並逐漸減緩。前 5 秒的震源時間函數整體大致呈三角形。由於去年 2018 年花蓮外海發生過 M6.1 的強震，造成花蓮地區嚴重人員傷亡與建物損毀，加上台灣東部 1951 年曾經連續發生多個規模 7 的地震，統稱花蓮地震序列。該地震序列的起始位置與這兩次花蓮地震的位置與地質背景均相當類似，後續台灣東部是否會有更大的地震發生，值得持續觀查與注意。</p> <p>附註：此研究成果已經發表於亞洲地球科學期刊(JAES):  <a href="https://www.sciencedirect.com/science/article/pii/S136791201930447X">https://www.sciencedirect.com/science/article/pii/S136791201930447X</a></p>
<p>計畫變更說明</p>	<p>(若有)</p>
<p>落後原因</p>	<p>(若有)</p>
<p>檢討與建議 (變更或落後之因應對策)</p>	

(以下接全文報告)

# **Strong ground motion over a large area in northern Taiwan caused by the northward rupture directivity of the 2019 Hualien earthquake**

Shiann-Jong Lee <sup>a</sup>, Tong-Pong Wong <sup>a</sup>, Ting-Yu Liu <sup>a</sup>, Tzu-Chi Lin <sup>a, b</sup>, and Chun-Te Chen <sup>a</sup>

<sup>a</sup> Institute of Earth Sciences, Academia Sinica, Taipei, Taiwan

<sup>b</sup> Department of Geosciences, National Taiwan University, Taipei, Taiwan

## **Abstract**

An  $M_w$  6.2 earthquake struck Hualien on the eastern coast of Taiwan on April 18, 2019. Its focal mechanism was determined to be a thrust fault with a depth of 18.8 km. A wide range of strong ground shaking with an intensity value from 4 (25 - 80 gal) to 7 (greater than 400 gal) occurred in northern Taiwan, which is unusual for earthquakes of this size. Here we show a source model as determined by local seismic waveform inversion. Two asperities were found, the smaller one occurred at the hypocenter and the larger one was found 10 km north of the hypocenter with a depth of 18 - 25 km. The initial rupture started from the hypocenter and then rapidly propagated all the way to the large asperity in the north. A near supershear speed of close to 4.0 km/s was found to have occurred during this northward rupture process. The inverted source model was evaluated using forward three-dimensional ground motion simulations. The results show strong agreement with island-wide observed displacement waveforms and peak ground acceleration for periods from 3.0 to 20.0 seconds. The rapid northward rupture caused a strong directivity effect coupled with the specific source radiation pattern, resulting in a large area of strong ground shaking in northern Taiwan, even though the Hualien earthquake was a moderately-sized event.

**Keywords:** Rupture directivity, source radiation pattern, rapid rupture speed, strong ground motion, 2019 Hualien earthquake

## 1. Introduction

A moment magnitude ( $M_w$ ) 6.2 earthquake struck the Hualien region of eastern Taiwan ( $121.54^\circ\text{E}$   $24.06^\circ\text{N}$ ) on April 18, 2019 (05:01:07 UTC). From the centroid solution of the Real-time Moment Tensor monitoring system (RMT, Lee et al., 2013), the mechanism of this event was determined to be a thrust with some left-lateral slip component.

The ground shaking near the source area was extremely strong, the largest intensity was observed in Hualien county with a maximum intensity 7 ( $> 400$  gal) on the Central Weather Bureau (CWB) intensity scale. Shaking of intensity 5 ( $> 80$  gal) was experienced in parts of northern Taiwan. Strong ground shaking also occurred in Taipei city with an intensity of 4 ( $> 25$  gal) and duration of more than 10 seconds, which was the highest intensity earthquake recorded in Taipei in the past ten years. Fortunately, no one died during this event and only two buildings in the city were damaged.

The 2019 Hualien earthquake occurred in a complex tectonic area. It is located at the western side of the northernmost part of Longitudinal Valley, which is a suture zone of the Eurasian Plate and the Philippine Sea Plate (Yu et al., 1997). Thousands of earthquakes occur in this area every year. During the period from October to December in 1951, three events with a magnitude larger than  $M7$  occurred along the Longitudinal Valley (LV) between Hualien and Taitung. This earthquake series is known as the 1951 Longitudinal Valley earthquake sequence. The epicenter of the 2019 Hualien earthquake was close to one of the 1951 events (Fig. 1). It is also of note that the hypocenter of this event was very close to the  $M_w$  6.3 Hualien earthquake that occurred in 2018. Due to this similarity in magnitude, epicenter location, and focal mechanism, there is concern about the possibility of similar large events to follow. It should also be noted that the depth of the 2019 event (18.8 km) was deeper than that of the 2018 event (6.31 km), but the 2019 event resulted in a wider range of strong ground shaking than is usual for earthquakes of such a moderate size (see Fig. 2).

In this study, we perform a source inversion by using local seismograms to analyze the rupture process in order to find out which kind of structure was involved in this event as

well as how this moderately-sized earthquake produced such a wide range of strong ground shaking in northern Taiwan.

## 2. Data and method

The local ground motion data were taken from two local seismic networks: the Broadband Array in Taiwan for Seismology (BATS) and the Central Weather Bureau 24-bit Seismic Monitoring Network (CWB 24-bit). The near source records were considered with an epicenter distance of less than 80 km in order to avoid complex 3D path effects resulting from local sedimentary deposits, such as the Taipei basin and Yilan Plain. All waveforms were integrated into displacement and aligned with the time of the event origin. A 60-second waveform time window was used in the inversion. The band-pass filter applied to the local seismic waveforms was 0.05 – 0.33 Hz. In total, 29 waveform records in E, N, and Z components, were used in the inversion (Fig. 3).

We used a parallel non-negative least squares method (Lee et al., 2006) for the source inversion problem  $\mathbf{Ax} = \mathbf{b}$ . Here,  $\mathbf{A}$  is the matrix of local Green's functions,  $\mathbf{b}$  is a vector of observation, and  $\mathbf{x}$  is the solution in which the seismic moment is released on each subfault. The inversion used 20 time windows, each was 0.4 seconds in length and overlapped for 0.2 seconds. To evaluate the waveform fitting, a misfit was defined as  $(\mathbf{Ax}-\mathbf{b})^2 / \mathbf{b}^2$ . The local Green's functions were calculated using the spectral-element method (SEM, Komatitsch et al., 1999) with the 3D Taiwan tomography model (Huang et al., 2014). The same filtered frequency bands used for the observation were applied to the synthetic Green's functions. The upper bound of the rupture velocity was set as 4.0 km/s, resulting in an inverted rupture speed that varied between 0 km/s and 4 km/s. A test of varying maximum rupture velocity is provided in the Appendix.

Two fault planes based on the focal mechanism reported by the RMT are shown in Figure 1a. One of them has a N-S strike, dipping to the west (strike 205°, dip 56°, Fault 1), and the other is a nodal plane with a NE-SW strike, dipping to the southeast (strike 62°, dip 40°, Fault 2). The two fault planes both have a length of 42 km and a down-dip of 39 km. They were decomposed into 182 subfaults, each 3 km in length and 3 km in

down-dip direction. Most of the aftershocks were located along the down-dip trend of Fault 1 (Fig. 1b). In addition, the inversion result of the NE-SW strike nodal fault plane (Fault 2) was worse than that of Fault 1 (see Appendix for more information). Thus, we focused on the inversion results of Fault 1 in the following discussion. The observations and synthetic waveform fitting of Fault 1 are shown in Figure 3.

### **3. Results**

#### **3.1 Slip distribution**

The resulting slip distribution shows a compact slip pattern that had a size of about 15 x 10 km<sup>2</sup> with two asperities on the fault plane (Fig. 4). The slip near the hypocenter (Asperity I) was concentrated of about 50 cm, which shows a thrusting movement. Asperity II, located in the northern area about 10 km from the epicenter, was the largest asperity on the fault plane. The slip at Asperity II was mainly a thrusting movement and had a slip of more than one meter. This concentrated slip area was located in the middle crust, approximately 18 to 25 km deep, which is deeper than the hypocenter (18.8 km). The slip in the entire rupture zone increased gradually with depth between the hypocenter and Asperity II. The centroid reported by RMT (the red open star in Fig. 4) was located between Asperity I (the hypocenter) and Asperity II. Both the compact slip zone and aftershock distribution show a northeast to southwest trend (Fig. 4a). Most of the aftershocks were located outside of the slip zone, with the remainder located around Asperity II. The average slip and the maximum slip of the fault were 38.3 cm and 101.8 cm, respectively. The stress drop was 3.27 MPa, assuming a representative circular fault model for slips larger than 10 cm.

#### **3.2 Rupture process**

The accumulated slip snapshot is shown in Figure 5. The initial slip was concentrated near the hypocenter, and then the rupture quickly propagated toward the north. It mainly ruptured on the northern fault plane, which produced strong northward rupture directivity from one to six seconds. The slip continued to rupture at deeper crust (20-25km), about 10 km north of the epicenter and gradually formed Asperity II. The rupture of this event was relatively fast. It started from the hypocenter and propagated



toward the north. To evaluate the rupture speed of this process, we plotted three reference rupture fronts with constant rupture velocities ( $V_r$ ) of 4 km/s, 3 km/s, and 2 km/s in Figure 5. The slip near the hypocenter occurred immediately after the reference rupture front with  $V_r = 3.0$  km/s passed through. After approximately two seconds, this rupture propagated through the RMT centroid with a speed of approximately 3 km/s. Then, the rupture quickly extended toward the northern area. The slip of Asperity II began to appear when the rupture front with  $V_r = 4$  km/s passed through; thus, it had a fast rupture speed of approximately 4 km/s. The average shear wave velocity of the middle-to-deep crust in this area (depth = 18 – 25 km) was approximately 3.8 km/s (Fig. 5). The typical rupture speed is usually taken as 80% of the local shear wave velocity. However, the rupture speed of Asperity II was faster than the typical rupture speed and could be very close to the local shear wave velocity.

A complex seismic moment release history can be found from the moment rate function (Fig. 4c). Several high-frequency peaks occurred during the first two seconds, and this was caused by the initial rupture (Asperity I) and northward propagation process. Between 2.0 to 4.0 seconds, there was a large number of moment releases with a peak at approximately 2.5 seconds. This is related to the burst of seismic energy releases from Asperity II. Some moment releases can be observed between 5.0 and 7.0 seconds, coming from the small slips in the northern area that occurred before the end of the rupture. The entire source time function closely resembles a triangle with a duration of about 7 to 8 seconds and a peak at approximately 2.5 seconds. The total seismic moment is about  $2.32 \times 10^{18}$  Nm, and this is equal to an earthquake size of Mw 6.18.

## **4. Discussion**

### **4.1 Island-wide ground motion simulation**

An island-wide three-dimensional ground motion simulation was performed using the spectral-element method (Komatitsch et al., 2004; Lee et al., 2008) to validate the inverted rupture model. We compared the synthetics with the BATS and CWB 24-bit vertical displacement waveforms in Figure 6a. The comparisons of E-W and N-S components are provided in the supplementary material Figure S1. For the period

between 3.0 and 20.0 seconds, most of the characteristics of the observed waveforms could be reproduced by the synthetics. The waveforms observed near the northern epicenter (e.g., stations NACB and ETLH) generally having large amplitudes compared to the stations located south of the epicenter (e.g., stations EGFH and HGSD). The strong ground motions recorded in northern Taiwan were also well modeled (e.g., stations NNSB, EWT, NWL, and NHDH). In western Taiwan, the shallow low-velocity sedimentary deposits may have amplified the ground shaking, resulting in greater discrepancies with the observations (stations WTK, NMLH, and HSN). The island-wide waveform misfit of the forward modeling for 3.0 to 20.0 seconds in the vertical component is 0.404.

The comparison between observed and synthetic peak ground acceleration (PGA) is shown in Figure 6b. The observed Palert data (Wu et al., 2013) were low-pass filtered below 0.33 Hz to compare with the synthetic PGA, which was simulated under 0.33 Hz. Most of the observed PGA characteristics could be reproduced by the simulation. Records in both the Yilan Plain and the Taipei basin displayed large PGAs due to amplification caused by the sedimentary deposits. Weaker PGAs were observed in most of southern Taiwan. These phenomena were reproduced by the synthetic PGA. In the Western Plain, the same result was observed as in the waveform comparison: the simulated PGA was weaker due to the velocity model not having sufficient resolution to reproduce the sedimentary amplification effect completely.

Overall, the synthetic waveforms and PGAs were comparable to observations on the island-wide scale, which indicate that the inverted finite-fault source model of the 2019 Hualien earthquake is able to adequately reproduce the low-frequency characteristics (0.33 Hz) of the ground movements.

#### **4.2 Source radiation pattern and rupture directivity**

From the snapshot analyses, it was determined that the rupture of this event mainly propagated toward the north. To investigate whether this unique rupture process can cause a strong directivity effect that could produce anomalous large ground motion in northern Taiwan, we further tested three different source models: an explosion, a double-couple, and a finite-fault. To avoid complex path and site effects, we set the

velocity model to be half-space and the mesh model to be flat without surface topography. The norm of the three components PGA (also called the ShakeMap) is presented in Figure 7. The explosion showed a simple concentric circles pattern from the epicenter (Fig. 7a) and this simple pattern was in line with our expectation. For the point double-couple source model (Fig. 7b), large PGA extended from the epicenter in the N-S and E-W directions. This result was due to the characteristic of the focal mechanism that caused the distribution of amplified ground motion to have a specific pattern. In the finite-fault model, the large PGA not only occurred along strike but also extended toward the northwest (Fig. 7c). As shown from the rupture snapshot analysis, the 2019 Hualien earthquake ruptured all the way to the north. This source characteristic can amplify the ground shaking in the rupture direction and form a strong directivity effect. The stations located north of the epicenter generally having large amplitudes compared to the stations located south of the epicenter could be due to this source rupture characteristic (Fig. 6a). Moreover, the source radiation of the finite-fault model was different from that of the point double-couple in which the amplified PGA occurred on the northwest side. From these results, we concluded that the strong shaking over a large area in northern Taiwan was not only due to the local sedimentary amplification effect, i.e. the large PGA observed in the Yilan Plain and Taipei basin, but also dominated by two source factors: the source radiation pattern and rupture directivity.

### 4.3 Coulomb stress change

To analyze the relationship between the 2018 and 2019 Hualien earthquakes, the Coulomb failure stress change,  $\Delta CFS$ , was calculated. Coulomb failure stress change describes the stress change on the receiver fault plane after the earthquake. It is calculated by the effective normal stress, shear stress and frictional strength of the material. In this study, we followed the method by King et al. (1994) and Stein (1999).

$$\Delta CFS = \Delta\tau_s + \mu(\Delta\sigma_n - \Delta p)$$

where  $\Delta\tau_s$  is the shear stress change;  $\Delta\sigma_n$  is the normal stress change on fault plane;  $\Delta p$  is the change of pore pressure;  $\mu$  is the friction coefficient of the rock material. A finite-fault source model of the 2018 event (Lee et al., 2018) was used in this analysis. The mechanism of the receiver fault is strike  $205^\circ$ , dip  $56^\circ$ , and rake  $67^\circ$ , assumed from the fault plane of the 2019 event, and the target depth was set to 20 km. The result

showed that the Coulomb stress pattern has a positive stress change in the source area of the 2019 event (Fig. 8a). This indicates that the 2019 event occurred at the area where stress had accumulated after the 2018 event. A weaker positive stress change was also found at the 2019 source area when the receiver fault was assumed from the other nodal plane (Fig. 8b). The  $\Delta CFS$  was further calculated to analyze the relationship between the 2019 mainshock source model and its aftershock distribution (Fig. 8c). Result showed that most of the aftershocks have occurred in the area where the  $\Delta CFS$  shows both increased and decreased. It indicates again that the mainshock and its aftershocks occurred on a complex tectonic region where several seismogenic structures could be involved. The  $\Delta CFS$  also increased along the Longitudinal Valley when considering the mechanism of 2019 Hualien earthquake, this west-dipping fault plane could be related to the Central Range Fault (Fig. 8b). On the other hand, the  $\Delta CFS$  decreased in the LV when the receiver fault was assumed from the east-dipping Longitudinal Valley Fault (Fig. 8d).

#### **4.4 Tectonic implication**

The finite-fault source inversion results showed that the 2019 Hualien event occurred on an N-S strike west-dipping fault plane that has a fault geometry close to the initial rupture plane of the 2018 Hualien earthquake (Lee et al., 2018). However, the rupture of the 2018 event occurred at a depth of about 0 - 15 km (Lee et al., 2018; Huang and Huang, 2018), which is much shallower than the 2019 event that ruptured mainly at a depth of 20 km. The aftershocks of these events were also located in different areas: the 2018 aftershocks occurred in the shallow crust of approximately 10 km depths (Kuo-Chen et al., 2018) and the 2019 aftershocks occurred inland in a deeper crust (Fig. 1). The RMT centroid moment tensor report (Lee et al., 2013) of 2018 event contains more strike-slip component with a large CLVD compared to the 2019 event which is close to a pure thrust double-couple source. In addition, the 2018 event was complex that ruptured on several fault segments (Ma and Wu, 2018) while the 2019 event was relatively simple that ruptured on a single fault plane. All of these results imply that the 2018 and 2019 Hualien earthquakes could have different source mechanism and occur on the different structural background. Figure 9 provides a conceptual northernmost LV tectonic model inferred from the 2018 and 2019 Hualien earthquakes. The Coastal Range bedrock is subducting northward beneath the Eurasian plate together with the

Philippine Sea plate. The N-S striking, west-dipping fault (Fault A in Fig. 9) is the initial rupture plane of 2018 event which is the boundary fault between the Coastal Range bedrock and Central Range bedrock. The rupture fault of the 2019 Hualien earthquake was in a lower crust and was dipping toward the west. Its representative seismogenic structure could be Fault B as presented in Figure 9. According to the hypothesis of lithospheric collision in Taiwan (Wu et al., 1997), this seismogenic structure is explained as the boundary fault between the Central Range bedrock and subducted oceanic lithosphere (Sibuet and Hsu, 2004; Shyu et al., 2016; Lee et al., 2018). Thus, the 2018 event (Fault A) and 2019 event (Fault B) belong to different structure faults because the tectonic settings on the two sides of these two boundary faults are different. We proposed that the Central Range fault could be a complex fault system that contains two branches, one is in the shallow crust (<15 km depth) and the other is in a deeper crust (~20 km depth). The two western dipping faults of the 2018 and 2019 events could have related to the northern extension of this Central Range fault system.

## **5. Conclusions**

The source model determined from local waveform inversion indicated a rapid northward rupture process with relatively simple slip characteristics on two asperities. A fast rupture was observed during the development of Asperity II, which had a rupture speed close to 4.0 km/s. These results indicated that the 2019 Hualien earthquake may have had a strong directivity effect that amplified the ground motion in the rupture direction. Forward ground motion simulations revealed that the source radiation pattern could also play an important role in amplifying ground motion in the northwestern area. Combining all of these investigations, we concluded that the strong ground motion occurred over a large area in northern Taiwan during the 2019 Hualien earthquake was caused by two source effects: the source radiation pattern and the rupture directivity. In addition, soft sedimentary deposits in the Yilan plain and Taipei basin could have further amplified local ground shaking. The results suggested that the static Coulomb failure stress change increased along the LV and a previous study of the 2018 Hualien earthquake also pointed to the same conclusion (Lee et al., 2018). It was noted that there is a structural gap between Fault A and Fault B (Fig. 9), and the background seismicity

also shows a gap in that area (Fig. 1). This seismic gap could result from the geometry change at the contact boundary between the Coastal Range and Central Range bedrocks, and it might extend into the northernmost Longitudinal Valley. Seismology studies have revealed that the seismic gap could be an area expected to have a large earthquake in the future (Nishenko, 1991; Nalbant et al., 2005; Jackson and Kagan, 2006). Thus, it is necessary to increase awareness of the possibility of large earthquakes in eastern Taiwan.

## Appendix

The inversion result of the nodal plane (Fault 2) is shown in Figure A1b. In this inversion, all the used data and inversion settings, including maximum rupture velocity and the number of time windows, were the same as those used in Fault 1 (Fig. A1a). The result showed a NE-SW slip pattern with several slip patches in the shallow fault plane. The largest slip occurred in the north from the epicenter. The inverted waveform misfit of the nodal plane was 0.209 which was larger than that of Fault 1 (misfit 0.192). We further performed the island-wide forward ground simulation based on the slip model of the nodal plane and calculated the waveform misfit between observations and synthetics. Result indicated that the misfit of forward synthetic waveform was 0.465, and again this was worse than that of Fault 1 (forward waveform misfit 0.404).

The tests of varying maximum rupture velocity ( $V_{max}$ ) of 3.0 km/s and 5.0 km/s are shown in Figure A1c and Figure A1d, respectively. The slip patterns of these two results were close to  $V_{max} = 4.0$  km/s (Fig. A1a) in which they all had a large asperity in the northern fault plane and a weaker slip near the hypocenter. The difference of inverted waveform misfits between  $V_{max} = 3.0$  km/s, 4.0 km/s and 5.0 km/s were small. However, the result of  $V_{max} = 4.0$  km/s provided the smallest misfit in the island-wide forward waveform modeling.

## References

- Chang, H.C., Lin, C.W., Chen, M.M., Lu, S.T., 1998. An Introduction to the Active Faults of Taiwan: Explanatory Text of the Active Fault Map of Taiwan. Scale 1:500,000. Special Publish of Central Geological Survey Taiwan, 10, 103.
- Huang, H.H., Wu, Y.M., Song, X., Chang, C.H., Kuo-Chen, H., Lee, S.J., 2014. Investigating the lithospheric structures beneath Taiwan region by nonlinear joint inversion of local and teleseismic P-wave data: Slab continuity and deflection. *Geophysical Research Letters* 41(18), 6350-6357.
- Huang, M.H., Huang, H.H., 2018. The complexity of the 2018 Mw6.4 Hualien earthquake in east Taiwan. *Geophysical Research Letters* 45(24), 13249-13257.
- Jackson, D.D., Kagan, Y.Y., 2006. The 2004 Parkfield earthquake, the 1985 prediction, and characteristic earthquakes: lessons for the future. *Bulletin of the Seismological Society of America* 96, S397–S409.
- King, G.C., Stein, R.S., Lin, J., 1994. Static stress changes and the triggering of earthquakes. *Bulletin of the Seismological Society of America* 84(3), 935-953.
- Komatitsch, D., Liu, Q., Tromp, J., Süß, P., Stidham, C., Shaw, J.H., 2004. Simulations of ground motion in the Los Angeles basin based upon the spectral-element method. *Bulletin of the Seismological Society of America* 94, 187–206.
- Komatitsch, D., Tromp, J., 1999. Introduction to the spectral-element method for 3-D seismic wave propagation. *Geophysical Journal International* 139, 806-822.
- Kuo-Chen, H., Guan, Z.K., Sun, W.F., Jhong, P.Y., Brown, D., 2018. Aftershock sequence of the 2018 Mw 6.4 Hualien earthquake in eastern Taiwan from a dense seismic array data set. *Seismological Research Letters* 90(1), 60-67.
- Lee, S.J., Chen, H.W., Liu, Q., Komatitsch, D., Huang, B.S., Tromp, J., 2008. Three dimensional simulations of seismic wave propagation in the Taipei basin with realistic topography based upon the spectral-element method. *Bulletin of the Seismological Society of America* 98, 253–264.
- Lee, S.J., Liang, W.T., Cheng, H.W., Tu, F.S., Ma, K.F., Tsuruoka, H., Kawakatsua, H., Huang, B.S., Liu, C.C., 2013. Toward real-time regional earthquake simulation I: real-time moment tensor monitoring (RMT) for regional events in Taiwan. *Geophysical Journal International* 87, 56-68.
- Lee, S.J., Lin, T.C., Liu, T.Y., Wong, T.P., 2018. Fault-to-Fault Jumping Rupture of the



- 2018 Mw 6.4 Hualien Earthquake in Eastern Taiwan. *Seismological Research Letter* 90(1), 30-39.
- Lee, S.J., Ma, K.F., Chen, H.W., 2006. Three-dimensional dense strong motion waveform inversion for the rupture process of the 1999 Chi-Chi, Taiwan, earthquake. *Journal of Geophysical Research* 111, no. B11308.
- Ma, K.F., Wu, Y.M., 2018. Preface to the focus section on the 6 February 2018 Mw 6.4 Hualien, Taiwan, earthquake. *Seismological Research Letter* 90(1), 15-18.
- Nalbant, S., Steacy, S., Sieh, K., Natawidjaja, D., McCloskey, J., 2005. Seismology: Earthquake risk on the Sunda trench. *Nature* 435(7043), 756–757.
- Nishenko, S.P., 1991. Circum-Pacific seismic potential – 1989–1999. *Pure and Applied Geophysics* 135, 169–259.
- Shyu, J.B.H., Chen, C.F., Wu, Y.M., 2016. Seismotectonic characteristics of the northernmost Longitudinal Valley, eastern Taiwan : Structural development of a vanishing suture. *Tectonophysics* 692, 295-308.
- Sibuet, J.C., Hsu, S.K., 2004. How was Taiwan created? *Tectonophysics*, 379, 159– 181.
- Stein, R. S., 1999. The role of stress transfer in earthquake occurrence. *Nature* 402(6762), 605.
- Wu, F., Rau, R.J., Salzberg, D., 1997. Taiwan orogeny: thin-skinned or lithospheric collision? *Tectonophysics* 274, 191-220.
- Wu, Y.M., Chen, D.Y., Lin, T.L., Hsieh, C.Y., Chin, T.L., Chang, W.Y., Li, W.S., Ker, S.H., 2013. A high-density seismic network for earthquake early warning in Taiwan based on low cost sensors. *Seismological Research Letter* 84(6), 1048–1054.
- Yu, S.B., Chen, H.Y., Kuo, L.C., 1997. Velocity field of GPS stations in the Taiwan area. *Tectonophysics* 274, 41 – 59.

## Figure Captions

Figure 1. (a) The location map of the 18 April 2019  $M_w$ 6.2 Hualien earthquake. The orange open star and beach ball indicate the epicenter and focal mechanism provided by the CWB earthquake report. The red open star and beach ball show the centroid location and focal mechanism provided by RMT. The black open star and gray beach ball show the epicenter and focal mechanism of the 2018 Hualien earthquake. Gray open star indicates one event of the 1951 Longitudinal Valley earthquake sequence. Pink circles are the aftershocks occurred within 12 days after the mainshock. Active faults in the northernmost Longitudinal Valley are shown with red lines. Purple and gray open rectangles indicate the two fault planes (Fault 1, Fault 2); their shallowest portion are shown by bold lines. (b) The fault along the profiles P1 (purple line) and P2 (gray line) labeled in (a). White, red and blue circles indicate the background seismicity ( $M_L > 2.0$  from 1990 to 2018), 2019 aftershocks, and 2018 aftershocks projected on P1 and P2 ( $\pm 5$  km width), respectively. A seismic gap as shown by pink dotted circle can be observed along P1 and P2.

Figure 2. Comparison of intensities between 2019 and 2018 Hualien earthquakes. The black stars indicate the epicenter of the two events. The color circles show the intensity taken from the Palert based on the Central Weather Bureau intensity scale.

Figure 3. Comparison between observation and synthetic waveforms: (a) east-west component, (b) north-south component, and (c) vertical component. The black lines are BATS and CWB 24-bit observations, and the red lines are synthetic waveforms. All the waveforms are in the type of displacement and a band-pass filter with the period between 3 and 20 seconds was applied. The maximum amplitude of the observed displacement waveform and misfit between observation and synthetic are shown at each station. The pink star and open rectangular are the epicenter and the fault plane projected to the surface, respectively

Figure 4. (a) Map view of the slip distribution of the 2019 Hualien earthquake. The CWB epicenter and RMT centroid are indicated with a black star and a red star respectively. The blue and gray open stars show the epicenters of the 2018 Hualien earthquake and one of the 1951 Longitudinal Valley earthquake sequence, respectively. White circles are the aftershocks ( $M_L > 2.0$ ) occurred within 12 days after the mainshock. (b) Slip distribution on the fault plane. Two asperities are marked with red rectangles. Vectors are the slip direction and the amount of slip on each subfault. (c) Moment rate function.

Figure 5. (a) Snapshots of cumulative slip. The black open star indicates the epicenter reported by CWB and red open star shows the centroid reported by RMT. The colored open circles are three reference rupture fronts with rupture velocity ( $V_r$ ) of 4.0 km/s, 3.0 km/s, and 2.0 km/s. Lower-right panel shows the shear wave velocity ( $V_s$ ) distribution on the fault plane. The information of  $V_s$  was taken from a 3D tomography model (Huang et al., 2014).

Figure 6. (a) Comparison between BATS, CWB 24-bit data and island-wide forward synthetic waveforms. The black lines are observations and red lines are synthetics. All the waveforms are in the type of displacement and a band-pass filter with the period between 3 and 20 seconds was applied. The maximum amplitude of the observed data and misfit between observation and synthetic are shown at each station. (b) Comparison between Palert data and island-wide forward synthetic peak ground acceleration for the frequency below 0.33 Hz. Color circles indicate the Palert observations and color background shows the synthetic. The blue star and open rectangular are the epicenter and the fault plane projected to the surface. Black lines are the active faults in Taiwan reported by the Central Geological Survey (Chang et al., 1998).

Figure 7. The norm of the three components PGA (ShakeMap) determined from three different source models: (a) explosion, (b) double-couple, and (c) finite-fault. The velocity model is set to be half-space and the mesh model is flat without surface topography. The simulated ShakeMap of (a) and (b) are determined by source half-duration of 2.5 seconds. Each of the ShakeMap is normalized

to one and multiplying the result by 100 to obtain a percentage.

Figure 8. The Coulomb stress changes. Four different cases were considered: (a) Coulomb stress changes caused by the 2018 Hualien earthquake and the receiver fault mechanism was the Fault 1 at depth 20 km, (b) Coulomb stress changes caused by the 2018 Hualien earthquake and the receiver fault mechanism was the Fault 2 at depth 20 km, (c) Coulomb stress changes caused by the 2019 Hualien earthquake and the receiver fault mechanism was Fault 1 at depth 20 km, and (d) Coulomb stress changes caused by the 2019 Hualien earthquake and the receiver fault mechanism was the east-dipping Longitudinal Valley Fault (strike  $25^\circ$ , dip  $60^\circ$ , rake  $45^\circ$ ) at depth 20 km. The green open rectangular is the fault plane of 2019 event projected to the surface.

Figure 9. Conceptual tectonic model for the northernmost Longitudinal Valley inferred from the 2019 Hualien earthquake. Blue dotted line shows the initial rupture plane of the 2018 Hualien earthquake (Fault A) which is the boundary fault between the Coastal Range and Central Range bedrocks. The red dotted line in a lower crust indicates the major rupture fault plane of the 2019 Hualien earthquake (Fault B), which is the boundary fault between the Central Range bedrock and subducted oceanic lithosphere. Gray dotted circle indicates the possible location of the seismic gap as shown in Figure 1.

Figure A1. (a) The inversion result of the Fault 1 with a  $V_{\text{rmax}} = 4.0$  km/s, (b) the inversion result of the Fault 2 with a  $V_{\text{rmax}} = 4.0$  km/s, (c) inversion result on the Fault 1 with a  $V_{\text{rmax}}$  set to 3.0 km/s, and (d) inversion result on the Fault 1 with a  $V_{\text{rmax}}$  set to 5.0 km/s. The CWB epicenter and RMT centroid are indicated with a black star and a red star respectively. While circles are the aftershocks occurred within 12 days after the mainshock.

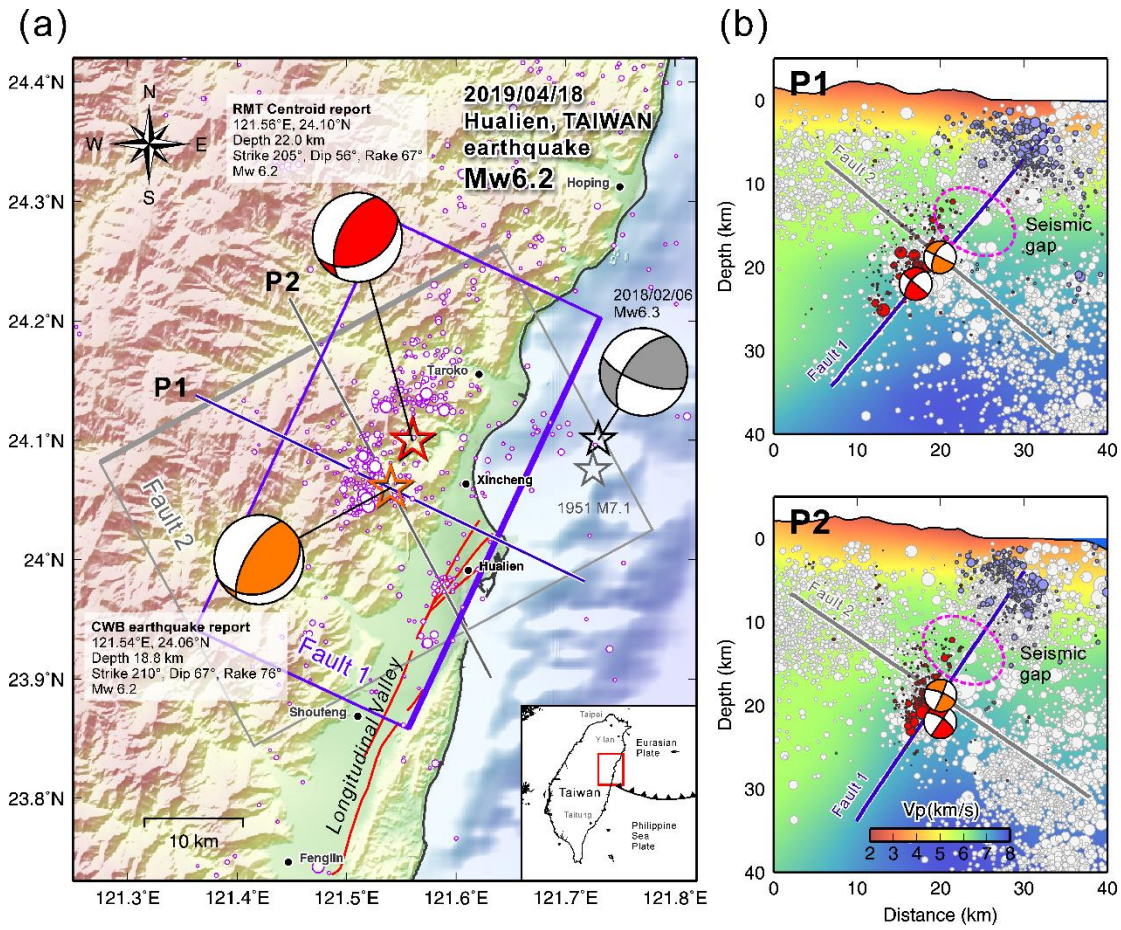


Figure 1. (a) The location map of the 18 April 2019  $M_w$ 6.2 Hualien earthquake. The orange open star and beach ball indicate the epicenter and focal mechanism provided by CWB earthquake report. The red open star and beach ball show the centroid location and focal mechanism provided by RMT. The black open star and gray beach ball show the epicenter and focal mechanism of the 2018 Hualien earthquake. Gray open star indicates one of the 1951 Longitudinal Valley earthquake sequence. Pink circles are the aftershocks occurred within 12 days after the mainshock. Active faults in the northernmost Longitudinal Valley are shown with red lines. Purple and gray open rectangles indicate the two fault planes (Fault 1, Fault 2); their shallowest portion are shown by bold lines. (b) The fault along the profiles P1 (purple line) and P2 (gray line) labeled in (a). White, red and blue circles indicate the background seismicity ( $M_L > 2.0$  from 1990 to 2018), 2019 aftershocks, and 2018 aftershocks projected on P1 and P2 ( $\pm 5$  km width), respectively. A seismic gap as shown by pink dotted circle can be observed along P1 and P2.

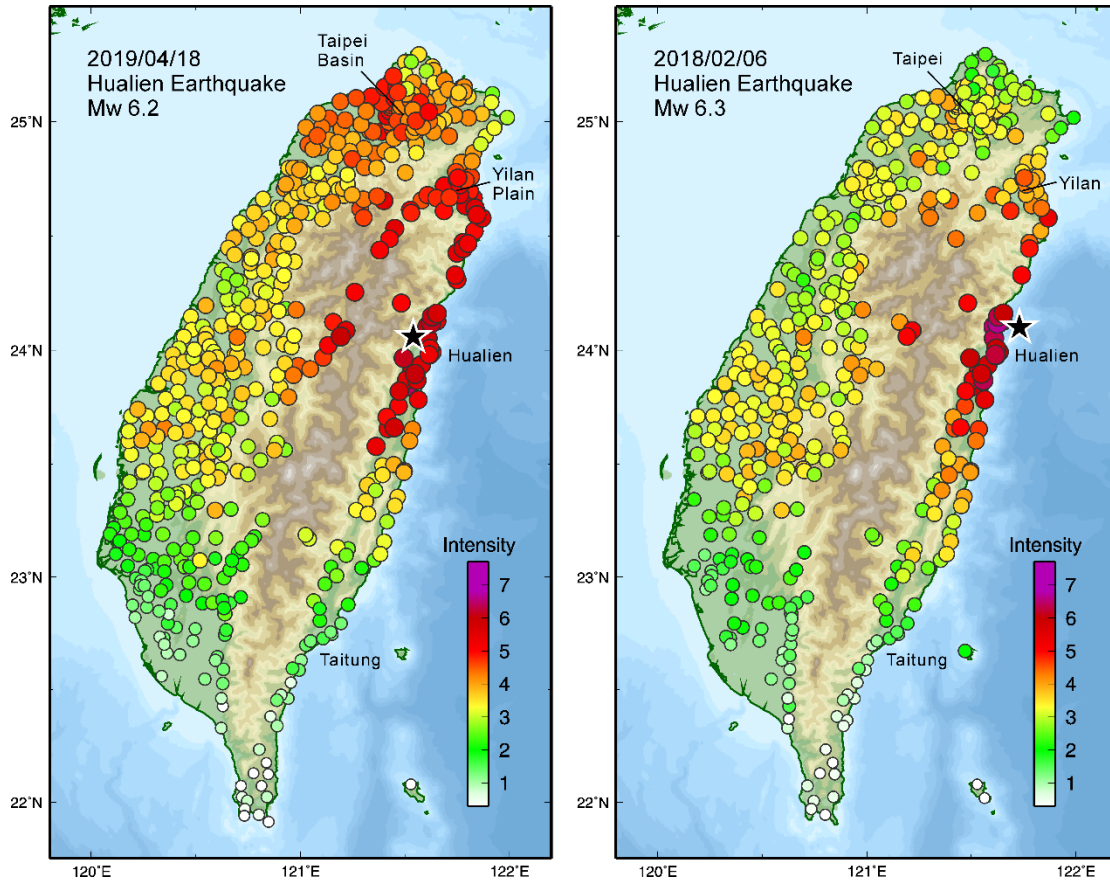


Figure 2. Comparison of intensities between 2019 and 2018 Hualien earthquakes. The black stars indicate the epicenter of the two events. The color circles show the intensity taken from the Palert based on the Central Weather Bureau intensity scale.

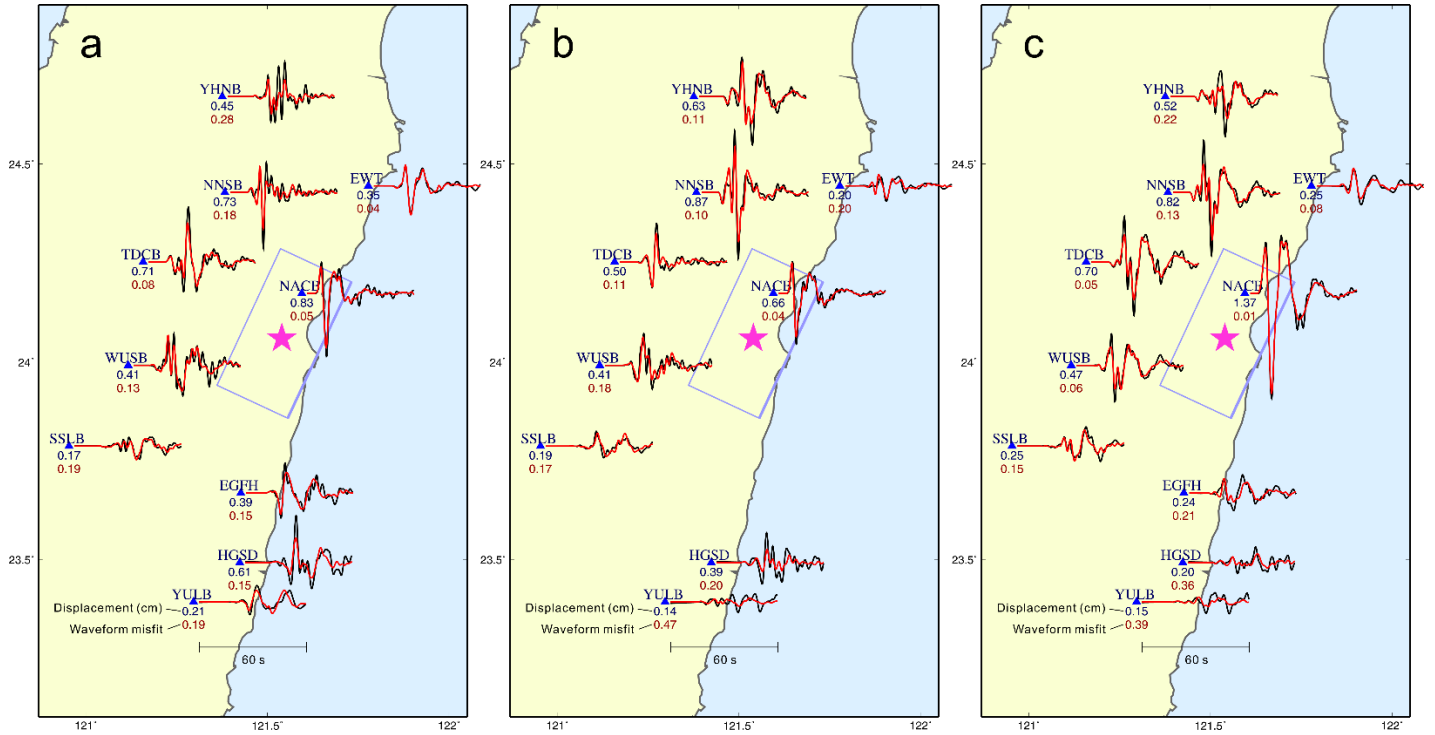


Figure 3. Comparison between observation and synthetic waveforms: (a) east-west component, (b) north-south component, and (c) vertical component. The black lines are BATS and CWB 24-bit observations, and the red lines are synthetic waveforms. All the waveforms are in the type of displacement and a band-pass filter with the period between 3 and 20 seconds was applied. The maximum amplitude of the observed displacement waveform and misfit between observation and synthetic are shown at each station. The pink star and open rectangular are the epicenter and the fault plane projected to the surface, respectively.

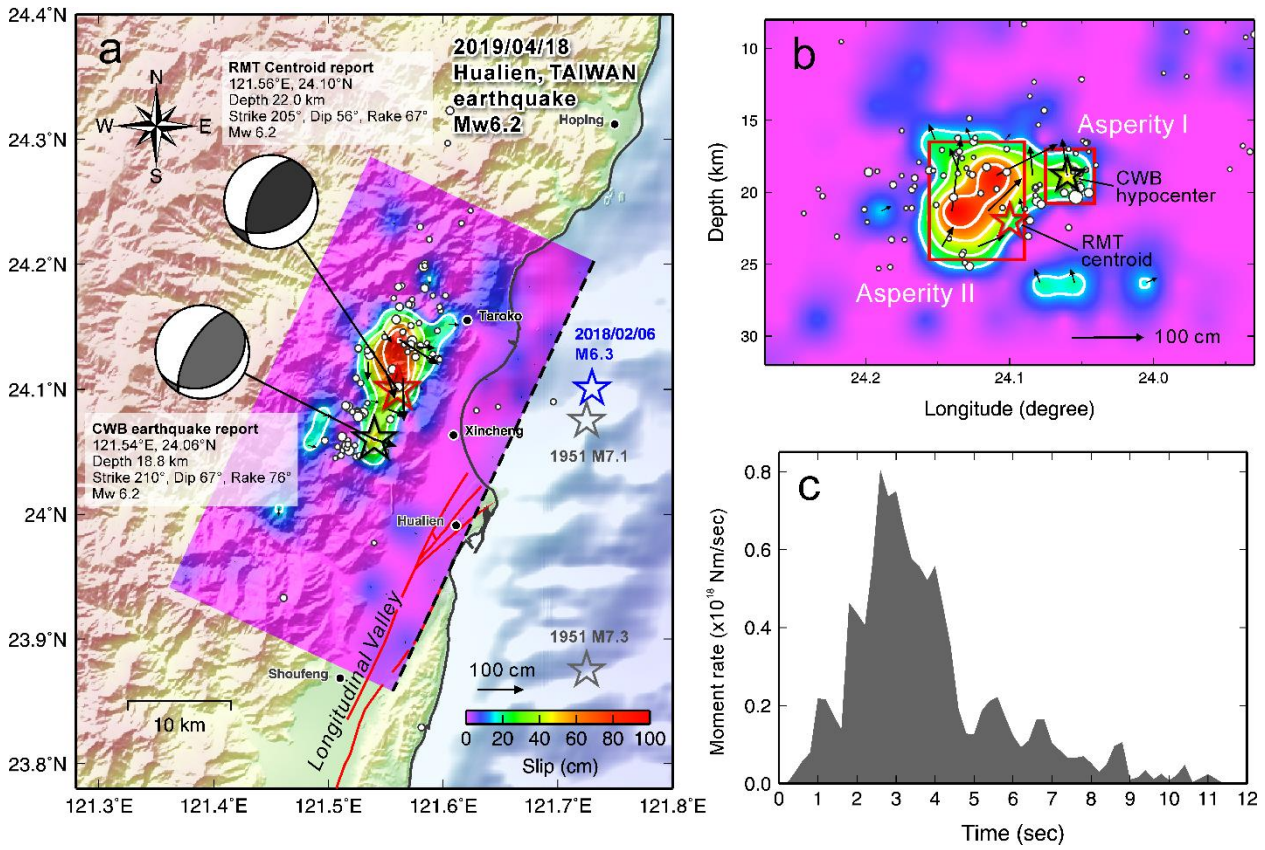


Figure 4. (a) Map view of the slip distribution of the 2019 Hualien earthquake. The CWB epicenter and RMT centroid are indicated with a black star and a red star respectively. The blue and gray open stars show the epicenters of the 2018 Hualien earthquake and one of the 1951 Longitudinal Valley earthquake sequence, respectively. White circles are the aftershocks ( $M_L > 2.0$ ) occurred within 12 days after the mainshock. (b) Slip distribution on the fault plane. Two asperities are marked with red rectangles. Vectors are the slip direction and the amount of slip on each subfault. (c) Moment rate function.



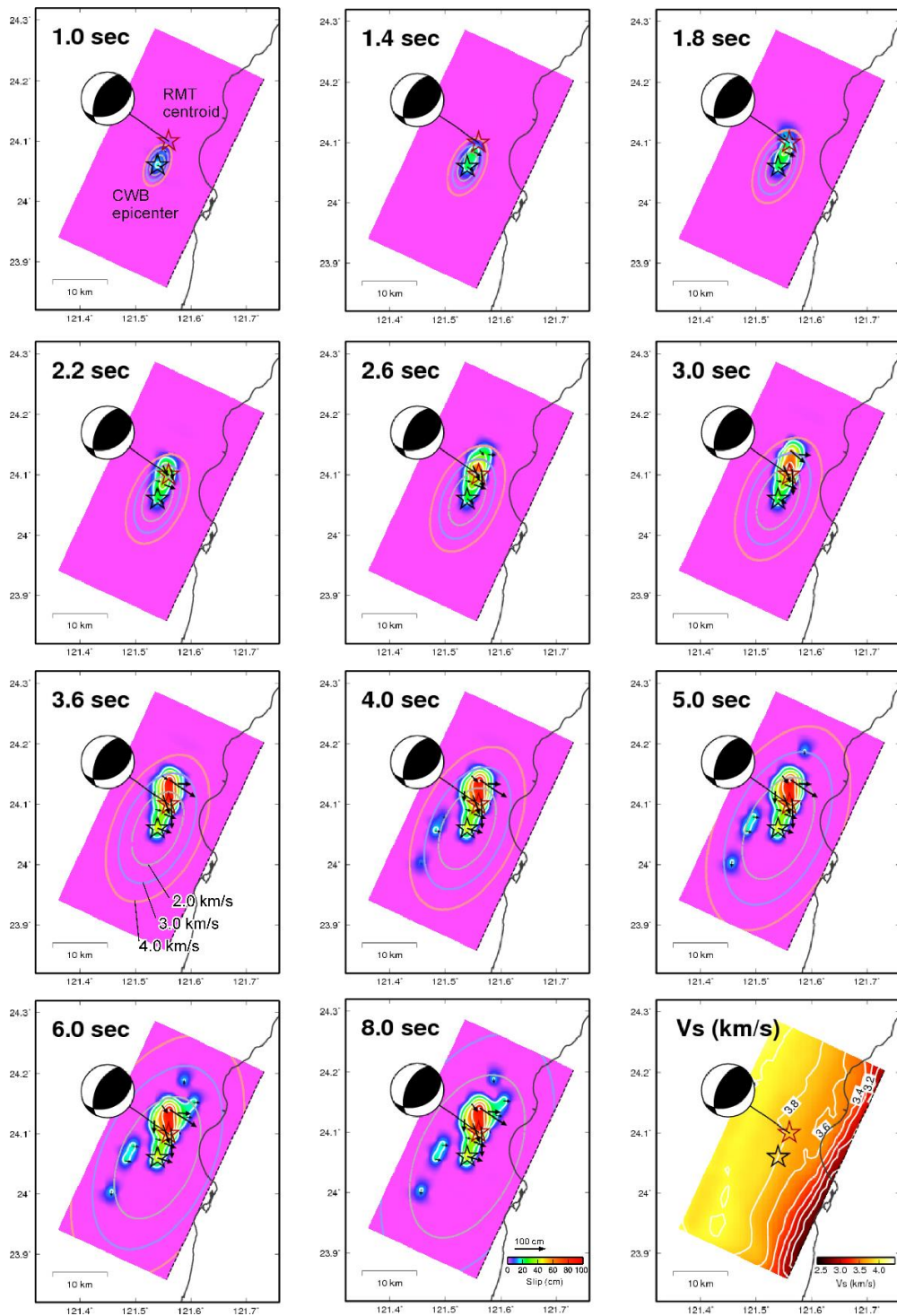


Figure 5. (a) Snapshots of cumulative slip. The black open star indicates the epicenter reported by CWB and red open star shows the centroid reported by RMT. The colored open circles are three reference rupture fronts with rupture velocity ( $V_r$ ) of 4.0 km/s, 3.0 km/s, and 2.0 km/s. Lower-right panel shows the shear wave velocity ( $V_s$ ) distribution on the fault plane. The information of  $V_s$  was taken from a 3D tomography model (Huang et al., 2014).

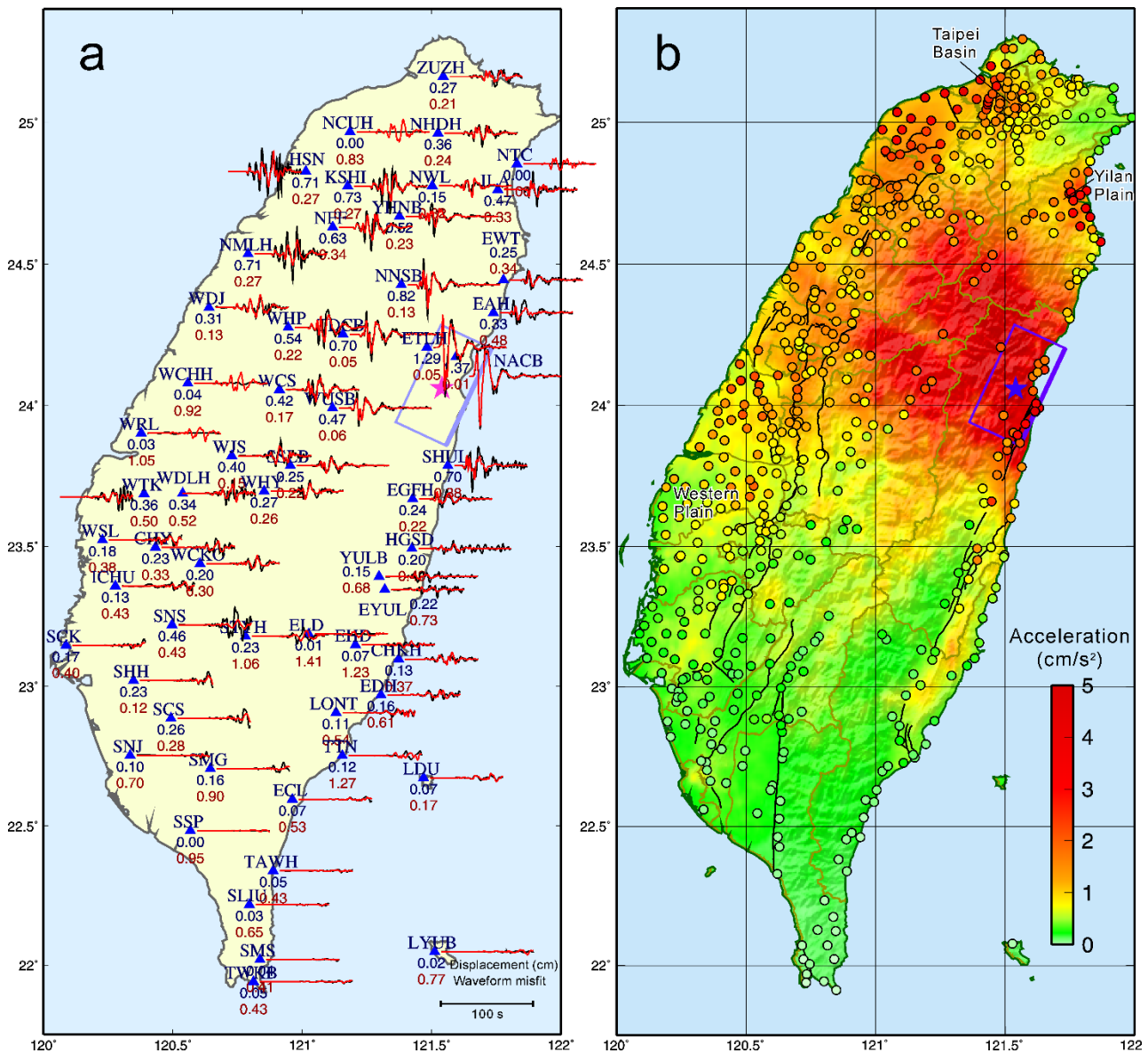


Figure 6. (a) Comparison between BATS, CWB 24-bit data and island-wide forward synthetic waveforms. The black lines are observations and red lines are synthetics. All the waveforms are in the type of displacement and a band-pass filter with the period between 3 and 20 seconds was applied. The maximum amplitude of the observed data and misfit between observation and synthetic are shown at each station. (b) Comparison between Palert data and island-wide forward synthetic peak ground acceleration for the frequency below 0.33 Hz. Color circles indicate the Palert observations and color background shows the synthetic. The blue star and open rectangular are the epicenter and the fault plane projected to the surface. Black lines are the active faults in Taiwan reported by the Central Geological Survey (Chang et al., 1998).

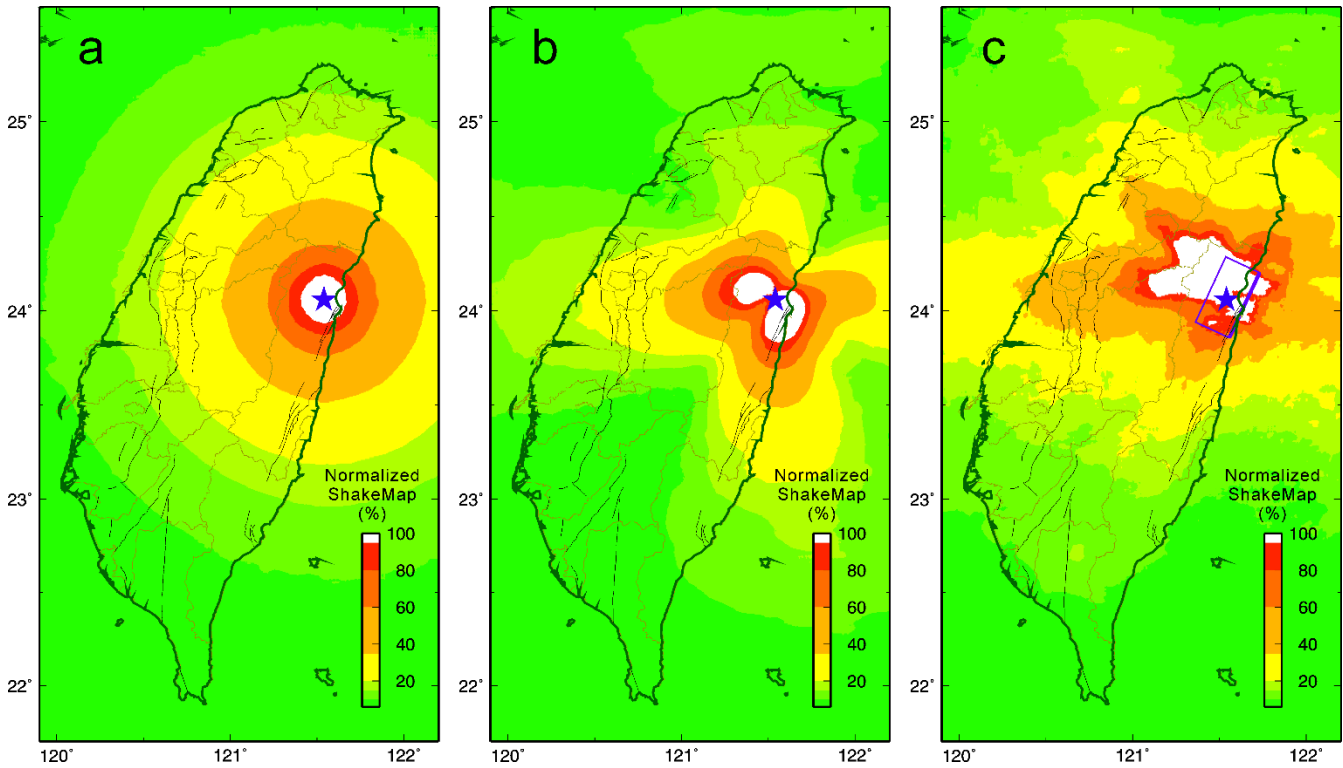


Figure 7. The norm of the three components PGA (ShakeMap) determined from three different source models: (a) explosion, (b) double-couple, and (c) finite-fault. The velocity model is set to be half-space and the mesh model is flat without surface topography. The simulated ShakeMap of (a) and (b) are determined by source half-duration of 2.5 seconds. Each of the ShakeMap is normalized to one and multiplying the result by 100 to obtain a percentage.

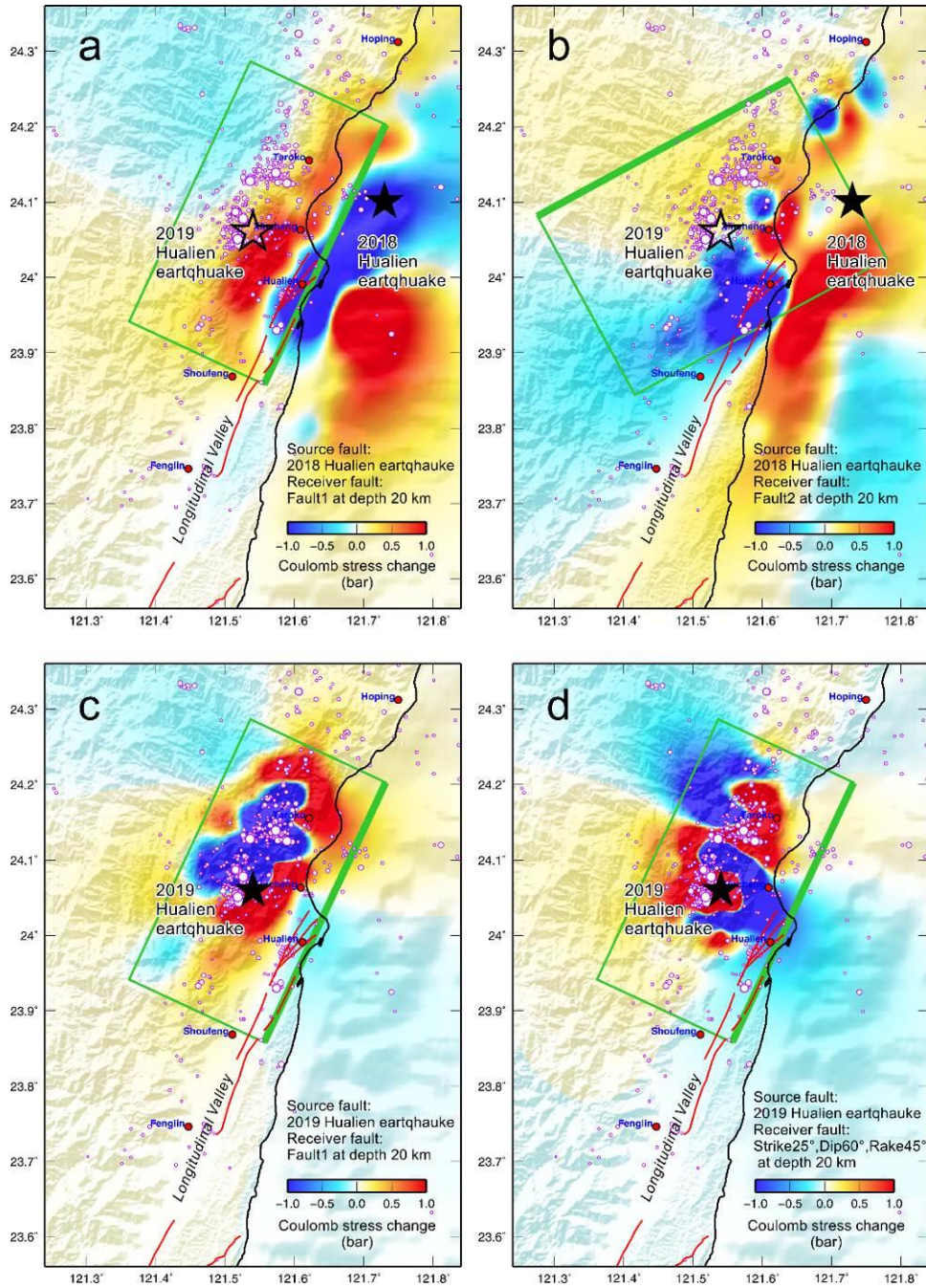


Figure 8. The Coulomb stress changes. Four different cases were considered: (a) Coulomb stress changes caused by the 2018 Hualien earthquake and the receiver fault mechanism was the Fault 1 at depth 20 km, (b) Coulomb stress changes caused by the 2018 Hualien earthquake and the receiver fault mechanism was the Fault 2 at depth 20 km, (c) Coulomb stress changes caused by the 2019 Hualien earthquake and the receiver fault mechanism was Fault 1 at depth 20 km, and (d) Coulomb stress changes caused by the 2019 Hualien earthquake and the receiver fault mechanism was the east-dipping Longitudinal Valley Fault (strike  $25^\circ$ , dip  $60^\circ$ , rake  $45^\circ$ ) at depth 20 km. The green open rectangle is the fault plane of the 2019 event projected to the surface.

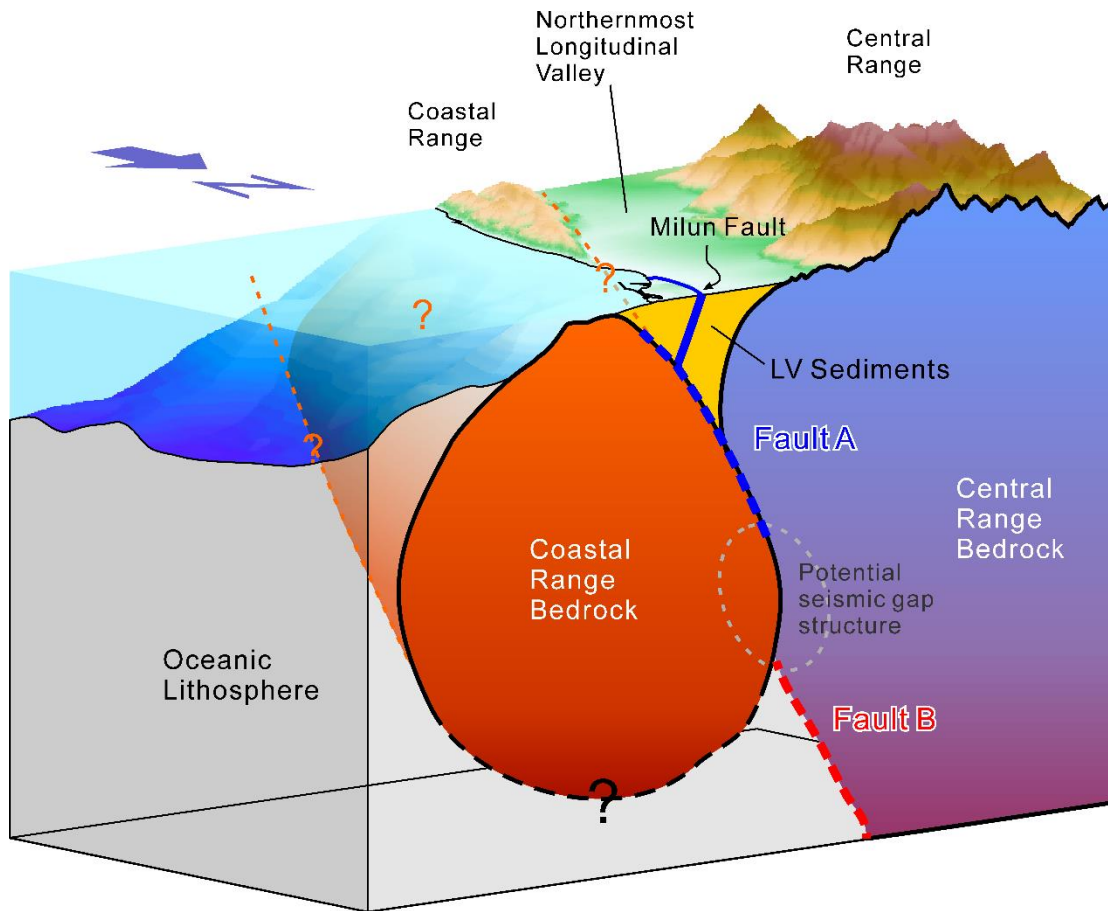


Figure 9. Conceptual tectonic model for the northernmost Longitudinal Valley inferred from the 2019 Hualien earthquake. Blue dotted line shows the initial rupture plane of the 2018 Hualien earthquake (Fault A) which is the boundary fault between the Coastal Range and Central Range bedrocks. The red dotted line in a lower crust indicates the major rupture fault plane of the 2019 Hualien earthquake (Fault B), which is the boundary fault between the Central Range bedrock and subducted oceanic lithosphere. Gray dotted circle indicates the possible location of the seismic gap as shown in Fig. 1.

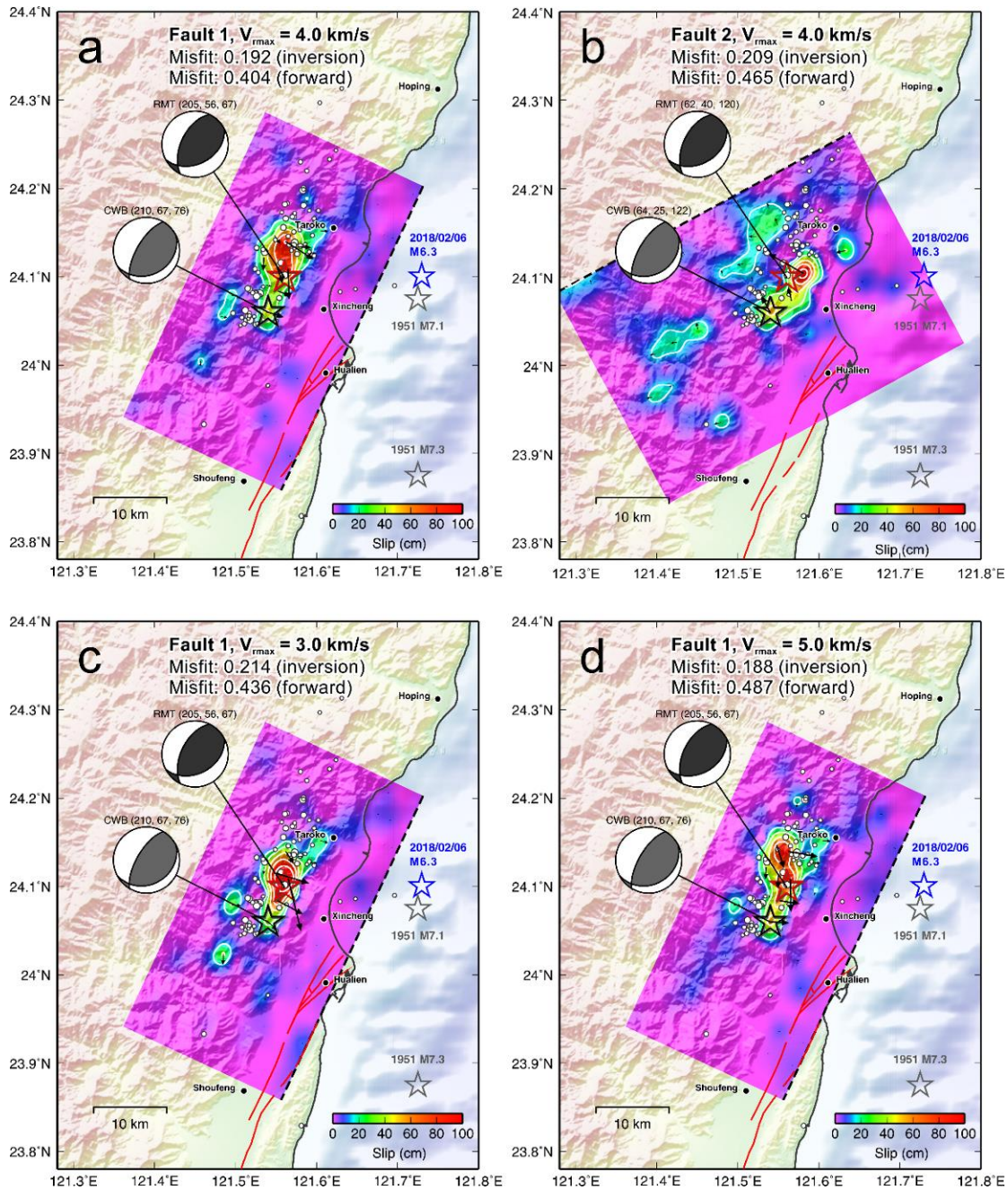


Figure A1. (a) The inversion result of the Fault 1 with a  $V_{\text{rmax}} = 4.0$  km/s, (b) the inversion result of the Fault 2 with a  $V_{\text{rmax}} = 4.0$  km/s, (c) inversion result on the Fault 1 with a  $V_{\text{rmax}}$  set to 3.0 km/s, and (d) inversion result on the Fault 1 with a  $V_{\text{rmax}}$  set to 5.0 km/s. The CWB epicenter and RMT centroid are indicated with a black star and a red star respectively. While circles are the aftershocks occurred within 12 days after the mainshock.

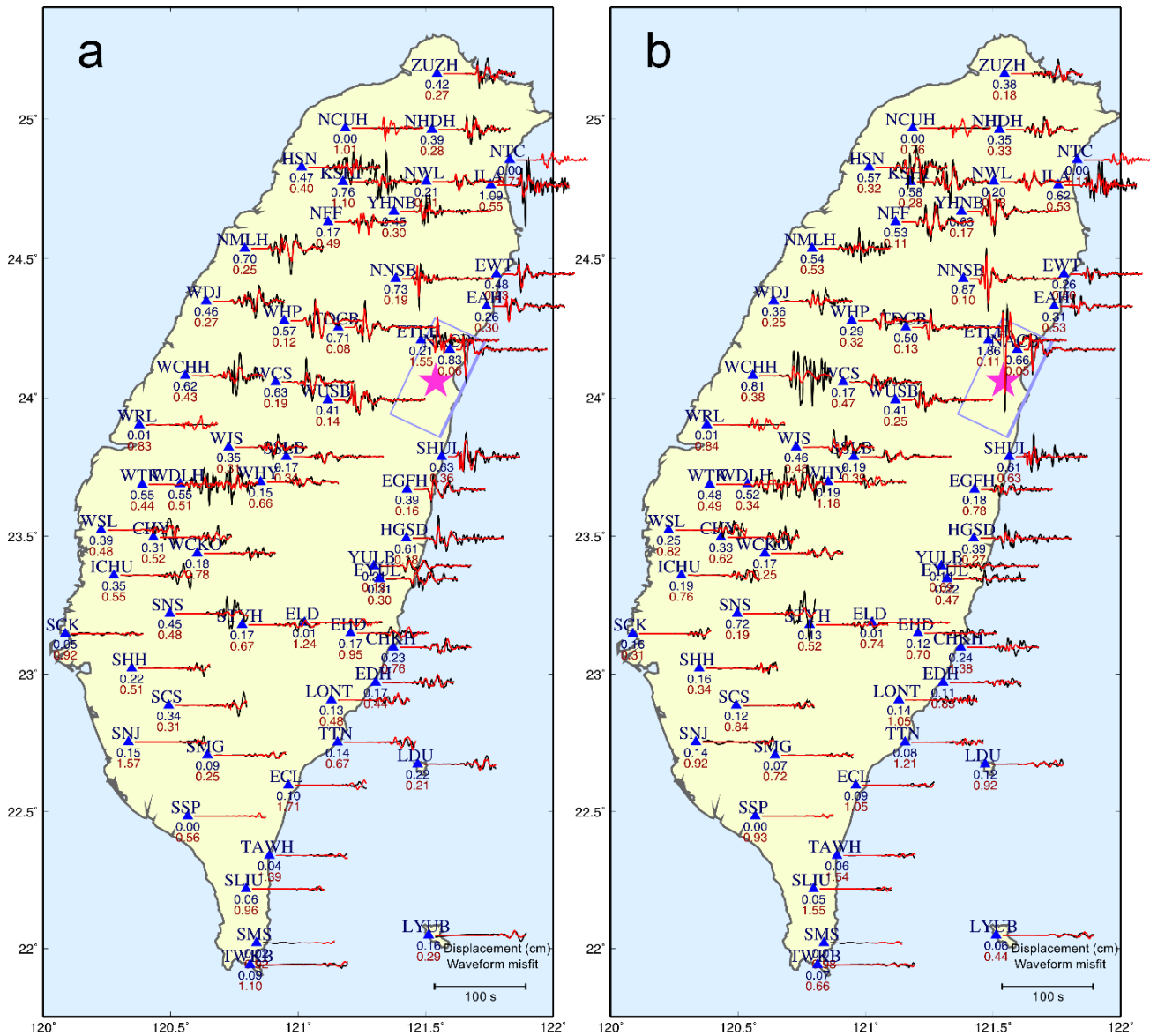


Figure S1. Comparison between BATS, CWB 24-bit data and island-wide forward synthetic waveforms. The black lines are observations and red lines are synthetics: (a) E-W component, and (b) N-S component. All the waveforms are in the type of displacement and a band-pass filter with the period between 3 and 20 seconds was applied. The maximum amplitude of the observed data and misfit between observation and synthetic are shown at each station. Pink star and purple open rectangular are the epicenter and the fault plane projected to the surface, respectively. The island-wide waveform misfit of the forward modeling for (a) E-W component and (b) N-S component are 0.675 and 0.594, respectively.

## 交通部中央氣象局

### 委託研究計畫(期中/期末)成果報告

#### 神經網路與深度學習在地震偵測上的應用

計畫類別：氣象    海象    地震

計畫編號：MOTC-CWB- 108 - E - 03 -

執行期間： 108 年 1 月 1 日至 108 年 12 月 31 日

計畫主持人： 金台齡

執行機構：台灣科技大學

本成果報告包括以下應繳交之附件(或附錄)：

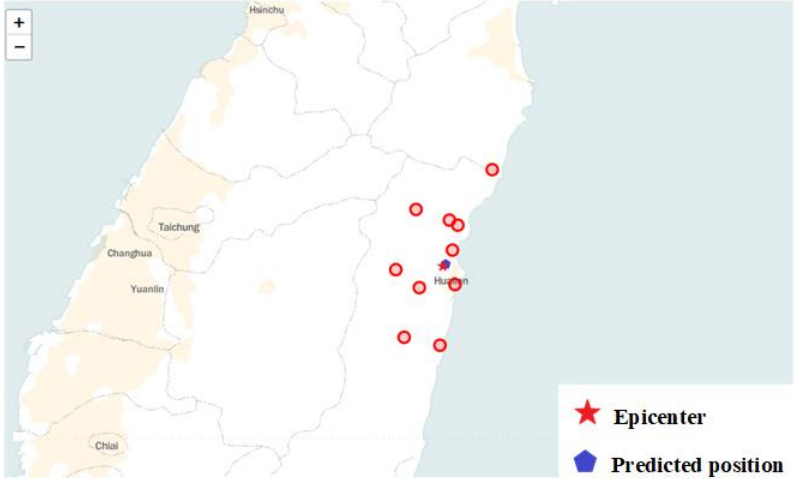
- 赴國外出差或研習心得報告 1 份
- 赴大陸地區出差或研習心得報告 1 份
- 出席國際學術會議心得報告及發表之論文各 1 份

中華民國 108 年 11 月 18 日



### 政府研究計畫(期中/期末)報告摘要資料表

計畫中文名稱	神經網路與深度學習在地震偵測上的應用		
計畫編號	MOTC-CWB-108-E-03		
主管機關	交通部中央氣象局		
執行機構	台灣科技大學		
年度	108 年度	執行期間	108/1/1 - 108/12/31
本期經費 (單位：千元)	304.304		
執行進度	預定 (%)	實際 (%)	比較 (%)
	95	95	0
經費支用	預定(千元)	實際(千元)	支用率 (%)
	304.304	304.304	100
研究人員	計畫主持人	協同主持人	研究助理
	金台齡		王德修
報告頁數	27	使用語言	中文
中英文關鍵詞	地震偵測、地震定位、類神經網路、人工智慧；Earthquake detection, earthquake localization, Neural network, Artificial intelligent		
研究目的	本計畫目的為利用中央氣象局於全台部屬的地震測站，藉由測站收集之資料搭配類神經網路演算法進行各式應用，其中包含利用遞迴式神經網路的即時地震即時預警、定位以及利用深度卷積網路進行的 P 波 S 波標記任務，盼望可以利用類神經網路演算法減少人工資料上的處理以及應用於即時系統上增強準確度。		
研究成果	本計畫中應用於定位的應用以 2018 年全年地震事件做為測試資料評估神經網路模型的效果，2018 年全年約 16199 筆事件，在震央位置上的誤差與中央氣象局紀錄的位置平均差距 4.78 公里，深度平均差距 4.56 公里，而在僅使用前 10 個收到 P 波之測站作為預測得到位置平均差距 4.83 公里，深度差距		

	<p>5.46 公里。而下圖為一範例，採用台北時間 2018/02/13 00:00 之地震紀錄，使用前 10 個收到 P 波之測站定位結果，圖中五邊形為實際震央，星形為本研究所定出之震央，圓形為測站。</p>  <p>而應用於即時預警的方法在測試中的時間誤差來到 0.149 秒優於傳統的方法 0.195 秒，且評估指標 True Positive Rate(TPR)及 False Positive Rate(FPR)中，TPR 以 0.991 優於傳統的 0.986，以及 FPR 0.018 優於傳統的 0.131。在應用於 P 波 S 波標記任務的方法目前在 P 波方面可以達到平均 0.16 秒的誤差，S 波方面則是 0.4 秒的誤差。</p>
<p>具體落實應用情形</p>	<p>本計畫採用類神經網路技術應用於地震定位、偵測、P 波 S 波標記，各方法皆有初步的成果，盼未來可以進一步實用。未來若有其他採用類神經網路用於地震方面的問題，本計畫之方法可提供參考。</p>
<p>計畫變更說明</p>	<p>(若有)</p>
<p>落後原因</p>	<p>(若有)</p>
<p>檢討與建議 (變更或落後之因應對策)</p>	

(以下接全文報告)

# 1 摘要

近幾年來，類神經網路的研究蓬勃發展，於各領域都有出色的表現，而本計畫主要研究如何將類神經網路應用於地震上，主要提出三種於地震上的應用，其中包含類神經網路於地震定位之應用，主要利用遞迴神經網路搭配注意力層於地震初期對震央進行判定，以及類神經網路於即時地震預警之應用，同樣利用遞迴神經網路即時地對波形進行偵測，接著深度卷積網路於 P 波 S 波檢測之應用，主要利用殘差網路及後續其他網路學習 P 波 S 波特徵位置進行 P 波 S 波位置判定。利用過去台灣收集到的地震震波資料，我們進行了實驗模擬評估所提方法之優劣，實驗結果顯示我們所提的方法在時間與準確度上優於傳統地震偵測的方法。

# 2 英文摘要

Recently, neural network technologies have been rapidly developed. Neural networks present excellent performance in many applications. This project develops three applications for earthquake detection by neural networks including earthquake detection and localization. For earthquake detection, recurrent neural networks have been used for real-time earthquake detection, while deep convolution neural networks have been used for P and S wave picking. For epicenter localization, an attention layer has been integrated with recurrent neural network for predicting epicenter in the early stage of earthquake occurrence. Extensive simulations were conducted to evaluate the performance of the developed schemes based on the collected earthquake waveforms in Taiwan. From the simulation results, the developed schemes outperform the traditional schemes in terms of time and accuracy.

### 3 前言

近幾年來類神經網路在各領域的研究皆有令人驚豔的成果，有許多種類神經網路結構被提出並應用於各種問題上，較常見的結構為卷積神經網路、遞迴神經網路、全連接神經網路，而各結構應用的方面也不同，例如卷積神經網路通常搭配全連接神經網路做分類任務，而遞迴神經網路則常應用於有時序關係的任務中，而本研究將這些不同結構的網路應用於地震偵測與定位問題中。

現有的類神經網路定位方法大多是利用卷積神經網路對地震波形圖學習後做出定位，但這樣的方法並不適用於即時系統中，故提出類神經網路於地震定位之應用，該方法運用遞迴神經網路的技術及注意力層，透過地震發生時各測所收到的 P 波到時及各測站收到 P 波事件的先後順序去判定出震央所在，如此便可以運用在即時系統上，將來可以於即時預警系統中提供更準確的震央位置，而該方法再利用前 10 個測站的資訊中可以達到 4.83 公里的位置誤差即 5.46 公里的深度誤差。

傳統在地震即時預警中的方法是需要往後等待 1~2 秒才能對該點進行判定，這樣的作法使得在 P 波到來時還是需要等待 1~2 秒才能發布警報，這 1~2 秒在分秒必爭的地震預警中相當的重要，因此提出類神經網路於即時地震預警之應用，使用了遞迴神經網路來達成即時 P 波 S 波偵測，因波形具有時序關係，故採用遞迴神經網路，該方法可以於地震的每一個時刻判斷 P 波 S 波機率，相對傳統需要往後取一段時間的做法更具即時性，而該方法最終可以達到 0.149 秒的時間差以及 99.1% 的準確度。

現行紀錄中的 P 波 S 波數據皆由人工辨識，為了減少人工辨識的工作量，提出了深度卷積網路於 P 波 S 波檢測之應用，利用深度卷積網路來找出 P 波 S 波於波形中的位置，主要由深度卷積從波形中學習特徵再由後續層來找出 P 波 S 波位置，目前結果達到 P 波有 0.2 秒左右誤差及 S 波的 0.4 秒誤差。

## 4 類神經網路於地震定位之應用

### 4.1 簡介

該研究主要在探討將類神經網路於地震定位上的應用，主要提出一類神經網路演算法可以在地震發生時即時的定出震央位置，盼該模型可以提供一個位置及深度上有著高準確的結果。類神經網路於即時地震預警之應用、

### 4.2 資料處理

用於訓練的資料取自中央氣象局紀錄，從 2016/1/1 至 2017/11/30，選取震央坐落於經度 120 至 122，緯度 22 至 25.5 且紀錄完整之事件，約 65000 筆事件，所用的測站為 CWB 觀測網中 211 個測站，如圖 1 所示，從每筆事件取出該事件震央之經度、緯度、深度、發生時間作為模型訓練的標記資料，接著取該事件收到 P 波的各個測站的經度、緯度、海拔、P 波到時，並依序排放整理成一個二維振列，用其當作模型輸入資料，最後將標記資料的發生時間及各測站收到的 P 波到時減去第一個收到 P 波的測站之 P 波到時，將其轉換為對第一個測站的時間差，因此標記資料中，地震發生的時間會標記為負值，輸入資料中 P 波到時都會是正值。

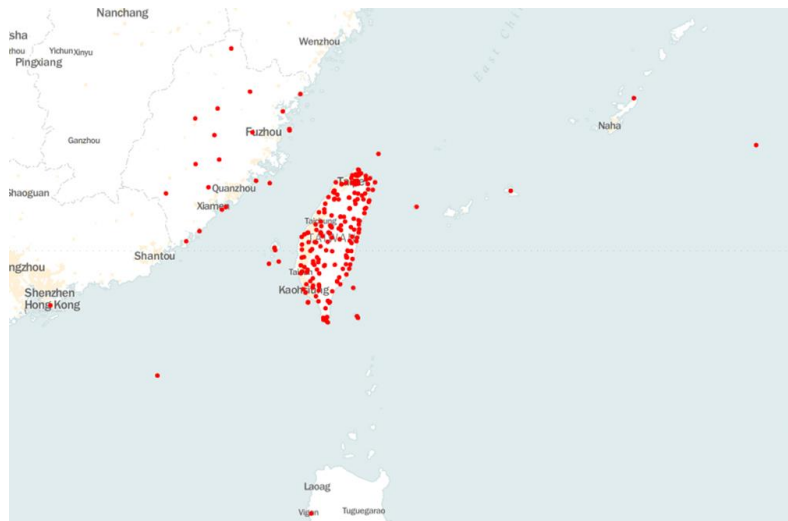


圖 1 CWB 觀測網測站分部圖

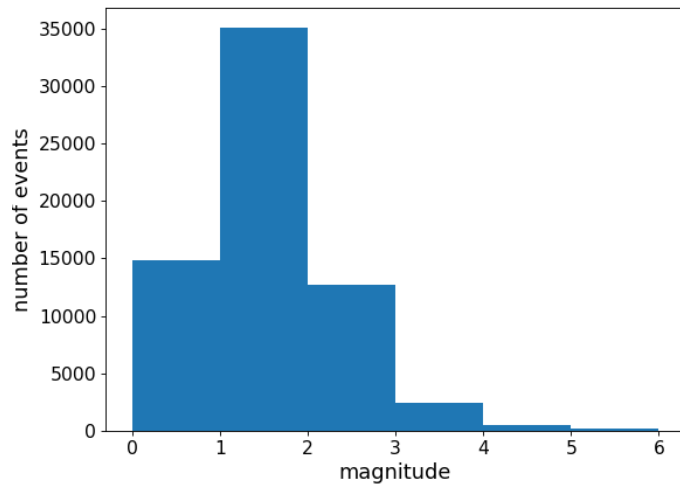


圖 2 訓練資料之規模分佈圖

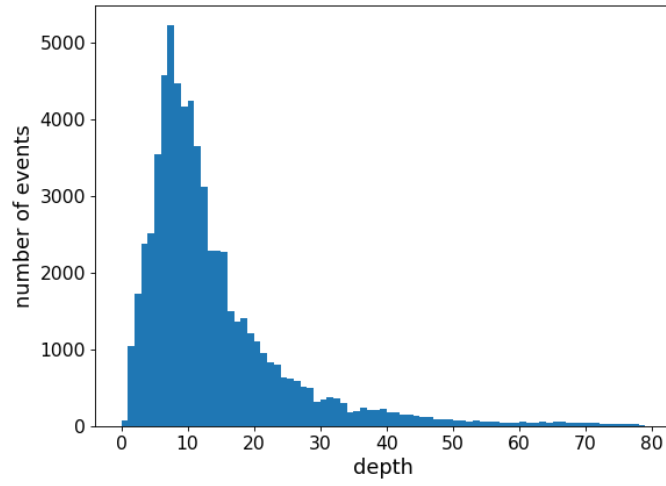


圖 3 訓練資料之深度分佈

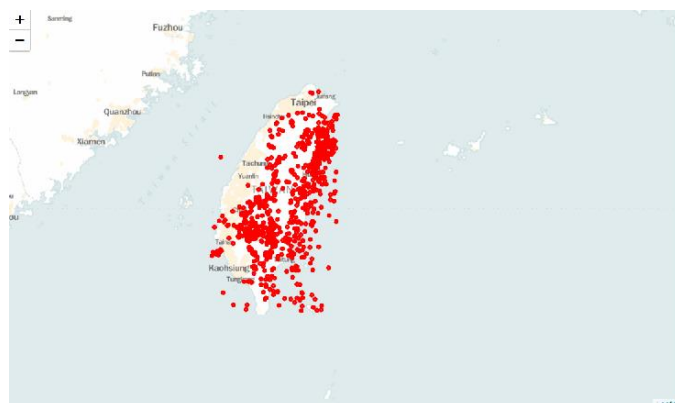


圖 4 訓練資料之震央分佈圖

圖 2 為訓練資料之規模分佈圖，可以看出小規模地震發生次數占多數，因平時小地震發生之次數較頻繁，而圖 3 為訓練資料之深度分佈，深度多數發生於 0~20 公里之間，而較深層之地震占少數，而淺層地震通常會造成較大傷害，而較多的淺層地震可以令類神經網路能更精準的判斷出淺層地震之深度，從而提高淺層地震預警時的準確度，而圖 4 為訓練資料之震央分佈，因事件過多，所以僅隨機取 1000 筆事件示意。

### 4.3 遞迴神經網路

本研究採用遞迴神經網路作為主要模型，遞迴網路與一般全連神經網路不同處在於遞迴神經網路會將前一時間點輸出資料當作當前時間點輸入資料從而將資料的序列性納入考量，而這樣普通的遞迴網路存在著一個問題，那就是無法有效的參照過久之前輸入的資料，故本研究採用另一種改良版的遞迴神經網路，LSTM(Long Short Term Memory)，架構如圖 5 所示，一個 LSTM 包含 Memory cell( $c_t$ )、Forget gate( $f_t$ )、Input gate( $i_t$ )、Output gate( $o_t$ )，Memory cell 用於儲存序列資訊，Forget gate 用於決定是否清空 Memory cell 中資訊，Input gate 用於決定當前輸入資料是否存入 Memory cell，Output gate 用於決定輸出何種資訊，藉由這些機制，在眾多實驗中，LSTM 表現優於普通的遞迴神經網路。

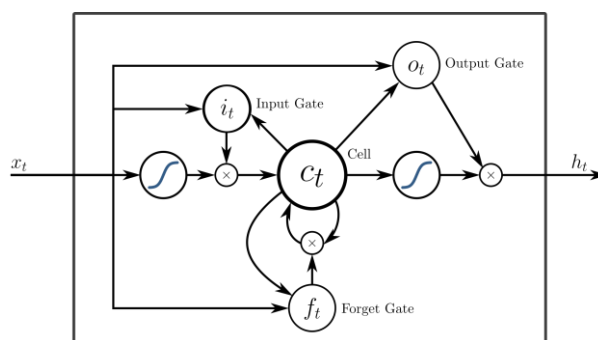


圖 5 LSTM 架構圖

### 4.4 模型架構

本研究模型整體架構如圖 6 所示，模型輸入端按 P 波到時順序輸入一地震事件所有收到 P 波的測站的經度、緯度、測站海拔、時間，而輸入的資料首先經過雙向 LSTM 層，雙向 LSTM 層由兩個 LSTM 組成，一個是正向 LSTM，一個是反向 LSTM，

正向 LSTM 如同字義上一樣，將輸入的資料由順著輸入的順序讀取，而反向則是將輸入資料由反方向讀取，其示意圖如圖 7 所示：

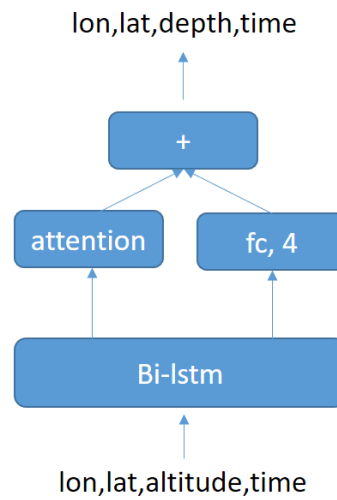


圖 6 模型架構圖

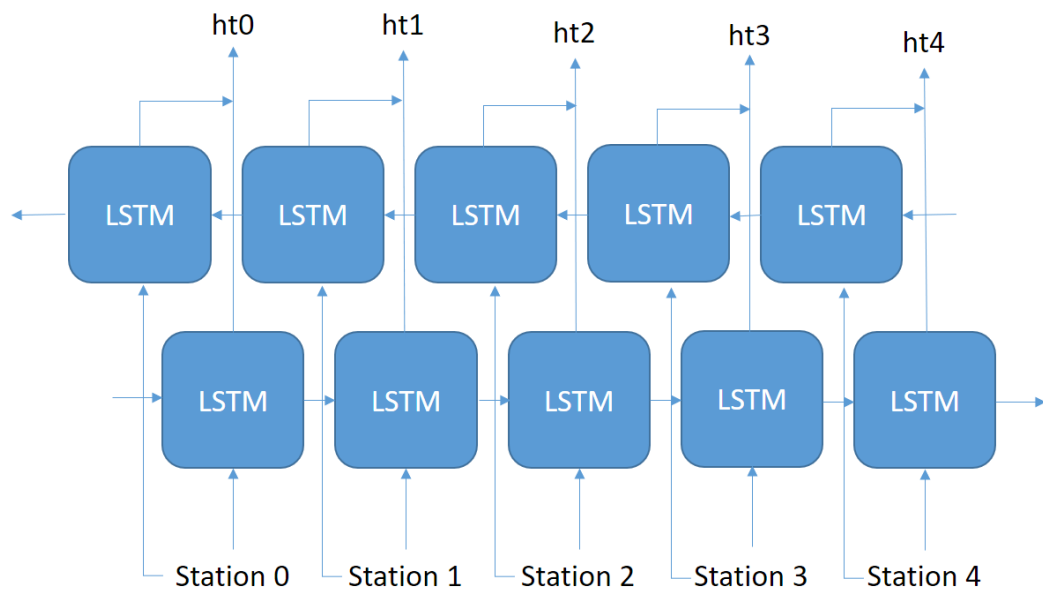


圖 7 雙向 LSTM



使用雙向 LSTM 是因為某個測站在事件中收到 P 波的原因可能跟早於該測站收到 P 波的測站有關係，也跟晚於該測站收到 P 波的測站有關係，故使用雙向 LSTM 使模型可以學習從最早收到 P 波的測站以及最晚收到 P 波的測站兩個方向進行學習，而本研究中採 3 層雙向 LSTM 各層皆含 64 個 LSTM 單元。

經過雙向 LSTM 後，可以得到模型讀取個個測站後的輸出，如圖 4 中的  $ht_0 \sim ht_4$ ，在此我們稱其為 hidden state，而在正向 LSTM 及反向 LSTM 讀取完各自的最後一個測站時得到前向的最後一個 hidden state 以及反向的最後一個 hidden state，得到這些輸出後，接著將其傳送到兩個層，分別是全連接層 (fully connected layer) 及注意力層 (attention layer)，全連接層的取 LSTM 層的前向、後向最後的 hidden state 串接為輸入，並輸出 4 個值，注意力層在自然語言處理中主要是用來對每個 hidden state 取權重後相加，得到一個新的 hidden state 再傳送到

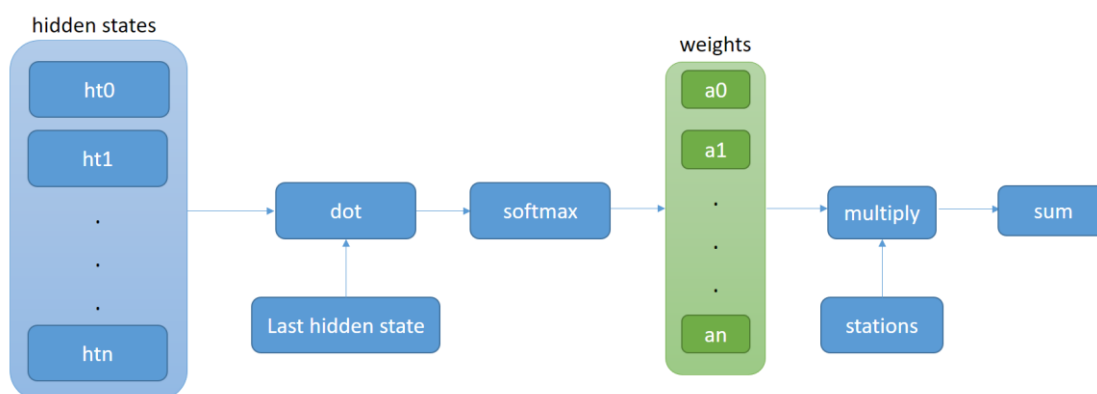


圖 8 注意力層架構圖

後續的層，此種做法可以有效解決遞迴神經網路無法記憶過久之前的資料的問題，而在此處也採用類似的作法，但此處的注意力層主要是用來模擬內插法，希望可以讓模型學習內插法的方法，對每個測站取比例下去修正出震央所在位置，而其詳細架構如圖 8 所示。

注意力層詳細步驟如下：

- 4.4.1 在取得由雙向 LSTM 層輸出的各測站的 hidden state 以及前後向的最後一個 hidden state 後，將前後向 hidden state 串接得到圖 5 中的 Last hidden state。
- 4.4.2 接著將 Last hidden state 與各個 hidden state 做內積。
- 4.4.3 做完內積後，會得到與測站數量等數量的  $n$  個輸出值，將這些值經 softmax 後可得每個測站的權重，如圖 5 中的  $a_0 \sim a_n$ 。

其中  $Z_j$  為  $j$  個 hidden state 與 Last hidden state 內積後的值，將其取指數後除以所有 hidden state 與 Last hidden state 內積取指數後的值之和，便完成 softmax 得到該測站之權重，其值介於 0~1 之間，如此將所有 hidden state 與 Last hidden state 內積後的值代入便可得所有測站之權重。

4.4.4 得到權重後，將權重個別乘回輸入的各測站的經度、緯度、海拔、P 波到時，並將各測站之值相加輸出 4 個值。在經過注意力層後，將其輸出之值與全連接層輸出之值相加，加完後過一激活層 ReLU (Rectified Linear Unit)，其式子如下，

$$f(x) = \max(x, 0)$$

將經緯度輸出限制為正值，接著將 4 個值中代表深度及時間的兩維乘上負號，將其輸出限制為負值，因深度以海拔 0 公尺為 0，而震央一定在海拔之下，而時間輸出與第一個收到 P 波測站的 P 波到時之時間差，故也一定為負值，到此，便可從模型得出震央的經度、緯度、深度、發生時間。

## 4.5 優化目標

訓練類神經網路模型時，採 mini batch 的方式訓練，一次取  $m$  筆事件做訓練，其模型優化目標如下：

$$\text{Minimize}(\alpha * \bar{e} + \beta * \bar{l} + \gamma * \bar{d})$$

其中  $\bar{e}$  為地震預警系統 TCPD 中用於定位的一項指標，其用意在於計算理論與觀測值的差距，當一地震發生，有  $n$  個測站收到 P 波，類神經網路模型輸出震央的經度、緯度、深度、發生時間  $T$ ，藉由這些資訊，可以經由 TCPD 中一套推測地震波行走時間的式子得到該推測震央到各個有收到 P 波的測站的行走時間  $t$ ，接著可以列出一個式子表示 P 波到時  $p$  與震央及震波傳遞時間的關係式如下，

$$p = T + t$$

意即推測出的震央之位置及發生時間要能與各站觀測到 P 波的時間符合上面式子，而推測出的震央即發生時間與 P 波觀測時間的誤差則為：

$$\bar{e} = \frac{1}{m} \sum_i^m e'_i$$

其中

$$e'_i = \frac{1}{n} \sum_k^n |e_k|$$

$\bar{e}$  即為對各測站之誤差值取絕對值平均後，在對每個 mini batch 取平均。距離的誤差與深度的誤差定義如下

$$\bar{l} = \frac{1}{2m} \sum_i^m |lr_i - lp_i| \quad \bar{d} = \frac{1}{m} \sum_i^m |dr_i - dp_i|$$

其中  $lr$  為標記資料中的震央經度、緯度， $lp$  為類神經網路模型輸出的經度、緯度， $\bar{l}$  即是將每筆事件標記震央減去預測震央取絕對值，而因經度、緯度有兩個值故取其合除 2，接著將每筆事件標記與預測之差取平均即為  $\bar{l}$ 。而  $dr$  為標記資料中的震央深度， $dp$  為類神經網路模型輸出的深度， $\bar{d}$  算法則為將每筆資料標記深度減去預測深度取絕對值，接著將每筆事件標記與預測之差取平均即為  $\bar{d}$ 。而  $\alpha$ 、 $\beta$ 、 $\gamma$  則為常數，用於調整訓練時對各個損失值的權重，而經實驗後目前設置值為  $\alpha=0.1$ ， $\beta=1$ ， $\gamma=0.005$ 。

## 4.6 訓練過程

訓練類神經網路模型過程中，使用 Adam 優化器，學習率一開始設置為 0.003，經 60 輪訓練後調整為 0.001，再經 60 輪訓練後調整為 0.0005，再經 60 輪調整為 0.0001 最後再經 60 輪便結束訓練。

## 4.7 具體成果

評估模型所用之資料為中央氣象局紀錄，取 2018 年整年定位品質 B 以上紀錄，且震央坐落於經度 120 至 122，緯度 22 至 25.5 之事件做測試，共 16199 筆事件，事件之詳細於下圖，資料前處理方法與章節 3.1 相同。接著是類神經網路模型於測試事件中，預測之震央位置、震央深度、發生時間與紀錄中震央位置、震央深度、發生時間之誤差。圖 9 為訓練資料之規模分佈圖，其中小規模地震發生次數占多數，而圖 10 為訓練資料之深度分佈，而圖 11 為測試資料之震央分佈，因事件過多，所以僅隨機取 1000 筆事件示意。

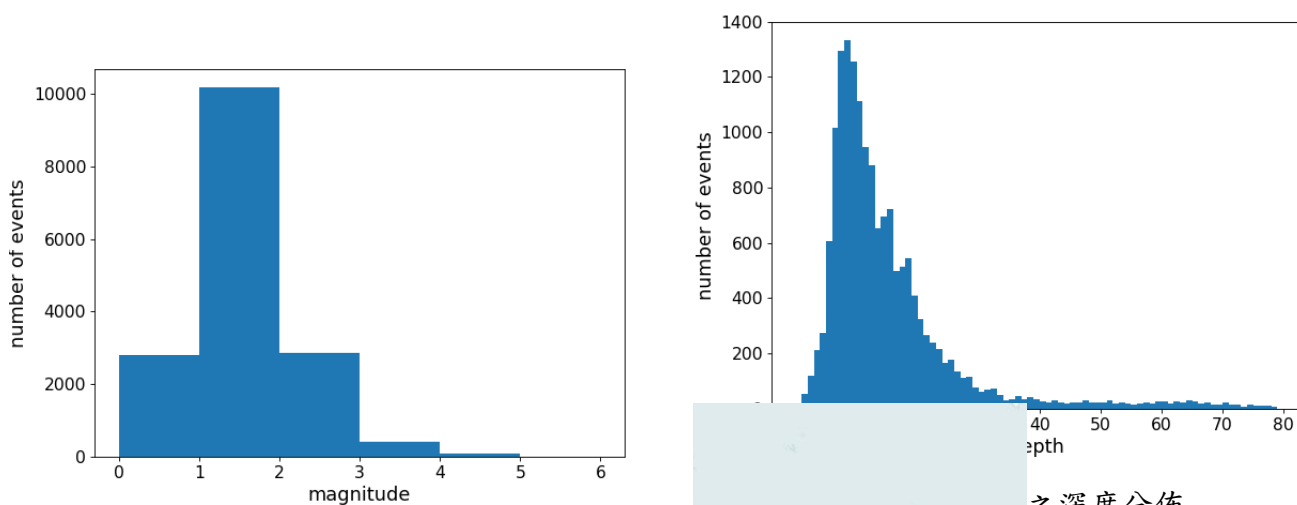
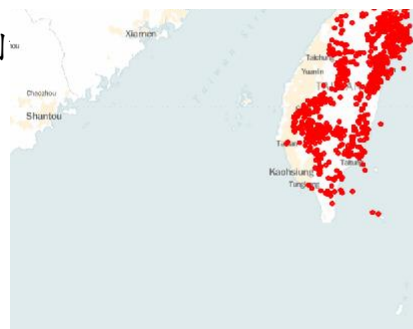


圖 10 測



之深度分佈

圖 11 測試資料之震央分佈

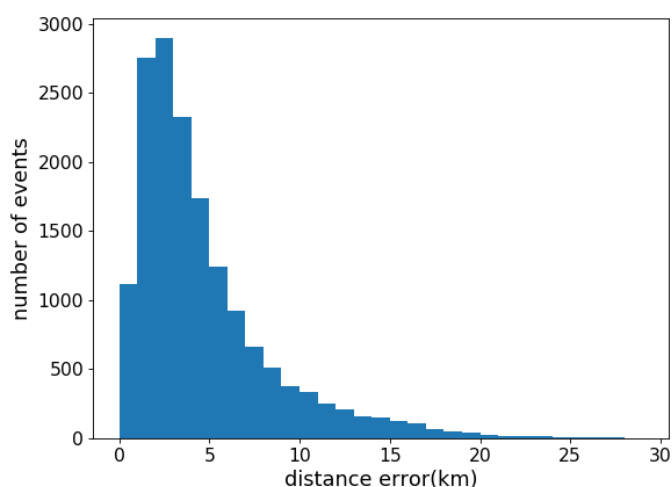


圖 12 震央位置誤差

圖 12 為類神經網路模型判定之震央與實際震央在距離上的誤差，在此測試中使用各個事件所有收到 P 波的測站去推測出結果，可以看到誤差大部分集中於 10KM 以下，5KM 以下更是占了多數，而 10KM 以上尚有些許事件，但占整體少數，整體誤差平均為 4.78 公里，而會有誤差的原因為本模型尚無法於訓練時達到位置判定的全局最佳解，故仍有誤差，盼未來能找出更佳模型令訓練時可以找到更佳解，使模型可以判斷出更佳的结果。

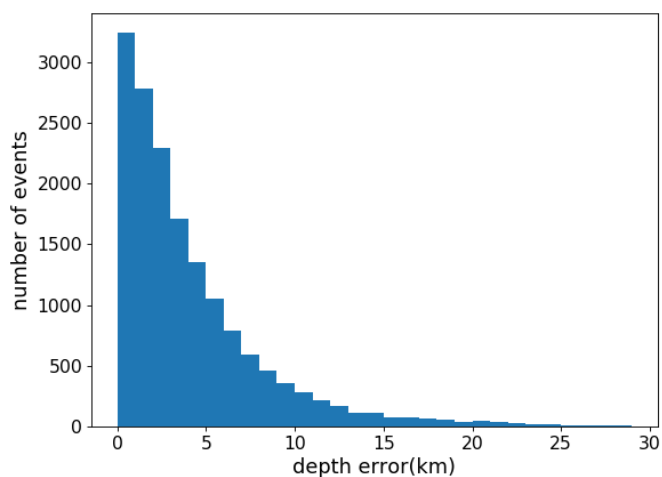


圖 13 震央深度誤差

圖 13 為類神經網路模型判定之震央與實際事件在深度上的誤差，在此測試中使用各個事件所有收到 P 波的測站去推測出結果，可以看到誤差大部分集中於 10KM 以下，5KM 以下更是占了多數，而接近 0KM 附近更是有最多資料分佈，整體誤差平均為 4.56 公里而會有誤差的原因為本模型尚無法於訓練時達到深度判定的全局最佳解，故仍有誤差，盼未來能找出更佳模型令訓練時可以找到更佳解，使得深度判定可以更準確。

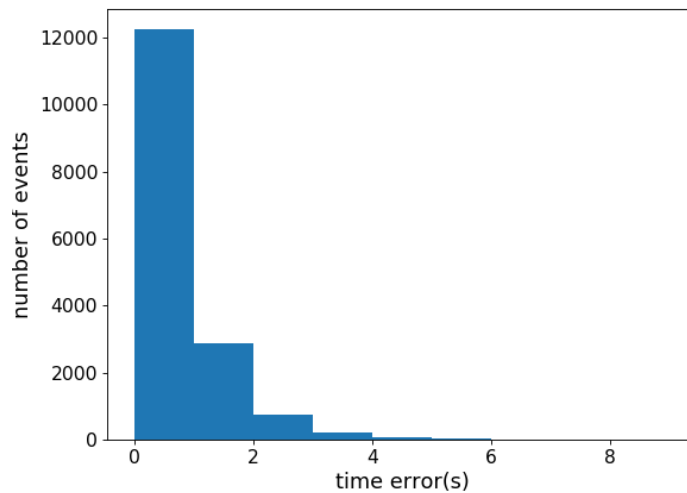
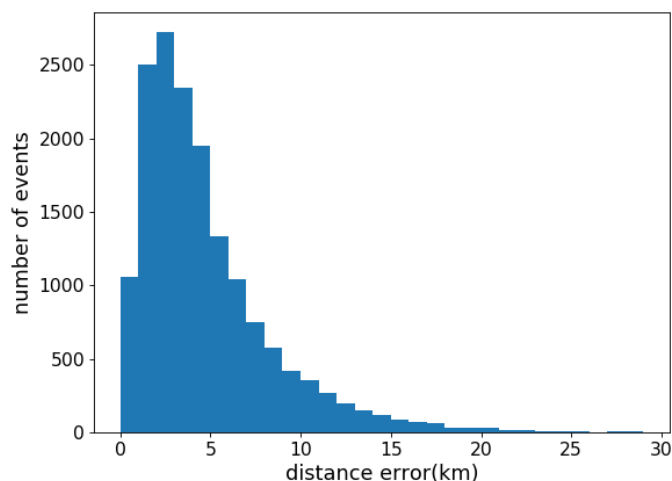


圖 14 發生時間誤差

圖 14 為類神經網路模型判定之震央與實際事件在發生時間上的誤差，在此測試中使用各個事件所有收到 P 波的測站去推測出結果，可以看到誤差大部分集中於 2 秒以下，而接近 0 秒附近之資料分佈占了整體多數，整體誤差平均為 3.18 秒而會有誤差的原因為本模型尚無法於訓練時達到時間判定的全局最佳解，故仍有誤差，盼未來能找出更佳模型令訓練時可以找到更佳解，以縮小誤差。

而本研究希望將  
法應用於即時預警  
中，故在實際使用中  
可能用所有測站之  
訊下去做判定，所以  
驗了僅用地震發生  
時，前 10 個收到 P

方  
不  
資  
實  
波



之測站下去做判定，這樣較符合實際場景，實驗結果如下。

圖 15 震央位置誤差(前 10 站)

圖 15 為類神經網路模型判定之震央與實際震央在距離上的誤差，在此測試中使用各個事件前 10 個收到 P 波的測站去推測出結果，可以看到誤差大部分還是集中於 10KM 以下，5KM 以下還是占了多數，但 10KM 以下占比可以看到有些許下降，表示在失去 10 站之後之測站資訊時，本方法在位置判定上會受到些許影響，但整體分佈情形變化不至於過大，整體誤差平均為 4.83 公里。

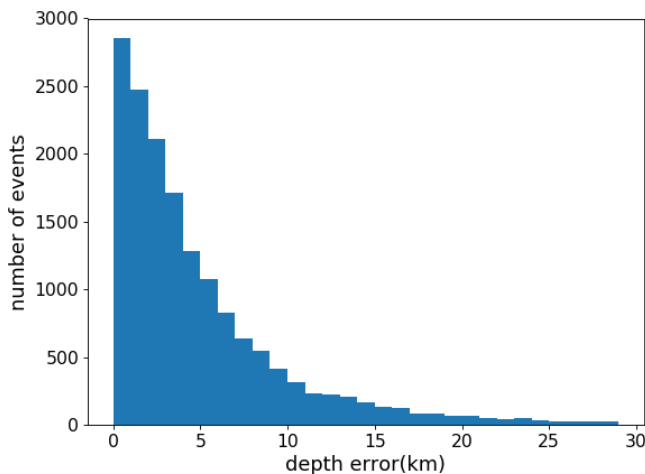


圖 16 震央深度誤差(前 10 站)

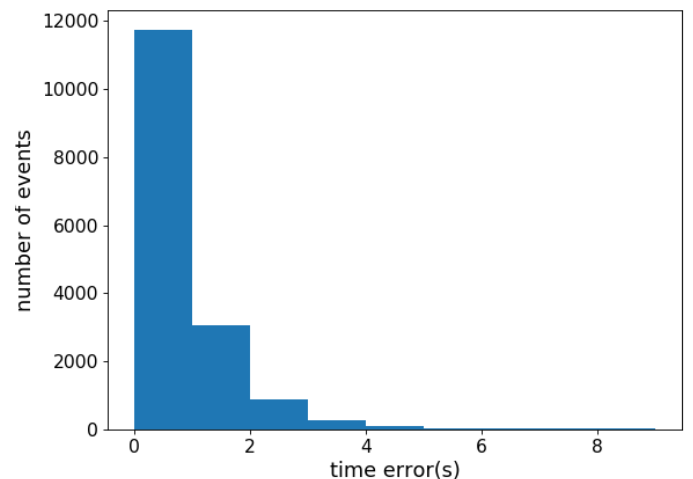


圖 17 發生時間誤差(前 10 站)

圖 16 為類神經網路模型判定之震央與實際事件在深度上的誤差，在此測試中

使用各個事件前 10 個收到 P 波的測站去推測出結果，可以看出整體分佈與用全部測站下去做判定之結果差不多，但在 10KM 以下之事件分佈數量略微變少，表示在失去 10 站之後之測站資訊時，本方法在深度判定上會受到些許影響，但整體分佈情形變化不至於過大，整體誤差平均為 5.46 公里。

圖 17 為類神經網路模型判定之震央與實際事件在發生時間上的誤差，在此測試中使用各個事件前 10 個收到 P 波的測站去推測出結果，可以看出整體分佈與用全部測站下去做判定之結果差不多，但整體誤差分佈略為往較大誤差的方向偏移，本方法在發生時間判定上會受到些許影響，但整體分佈情形變化不至於過大，整體誤差平均為 3.26 秒。

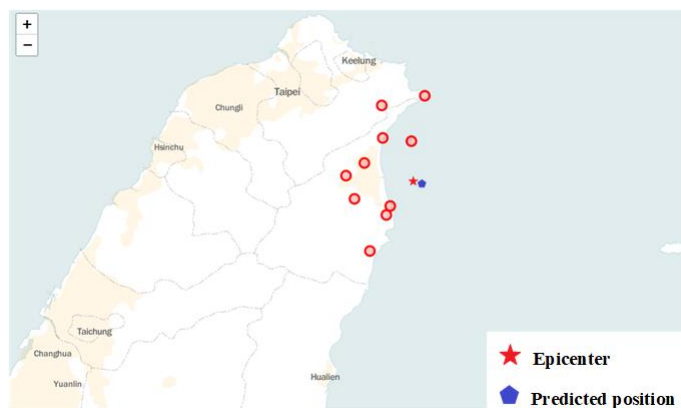


圖 18 實際震央與預測震央示意圖(1)

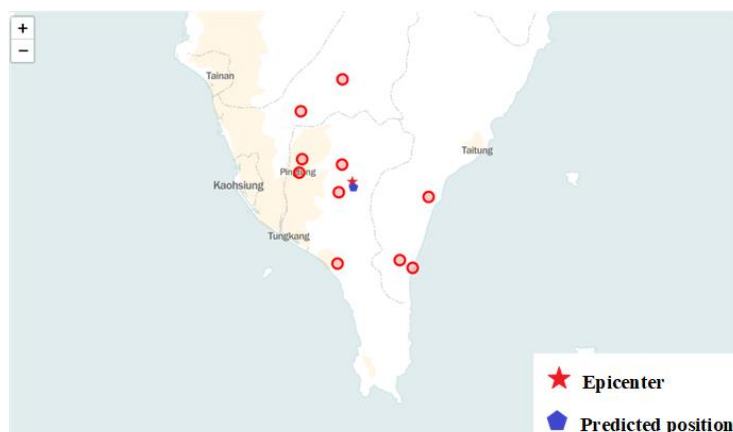




圖 19 實際震央與預測震央示意圖(2)

圖 18 為台北時間 2018/03/19 00:00 之事件、19 為台北時間 2018/08/16 04:40 之事件，而兩圖皆為類神經網路模型輸出之震央位置與實際震央位置示意圖，途中圓形為測站該事件前 10 個收到 P 波的測站，星形為實際震央，五邊形點為類神經網路模型使用前 10 個收到 P 波之測站所預測之震央，在這兩個例子中，可以看到實際震央與預測出的震央距離接近。

## 4.8 結論

本研究主要以遞迴神經網路及注意力層為模型主體，當一地震發生時，將收到 P 波之測站的經度、緯度、海拔、P 波到時，並按收到 P 波順序排列，將其輸入模型即可判斷出震央位置、深度及發生時間，而於測試中，模型判斷之震央與實際震央在大部分狀況都很接近。而在未來應用於預警系統中，可以提供準確的參考。

## 5 類神經網路於即時地震預警之應用

### 5.1 簡介

本研究主要探討如何將類神經網路方法應用於即時地震預警系統上，期望可以以類神經網路的演算法提供一個模型可以準確的在 P 波 S 波到來時發出警報，且盼該模型可以減少噪音對警報的影響，降低誤報率，同時也希望模型可以有好的召回率，意旨可以精準地找出 P 波 S 波的發生。

### 5.2 資料處理

本研究中使用資料來自 palert 地震網，圖 20 為 palert 地震網測站分布圖，研究中從 2016 至 2017 共取 128 個地震事件，其中包含 1797 個地震波形圖以及 1854 個雜訊波形圖，圖 21 為所用事件之震央分布圖，表 1 為各規模波形統計。

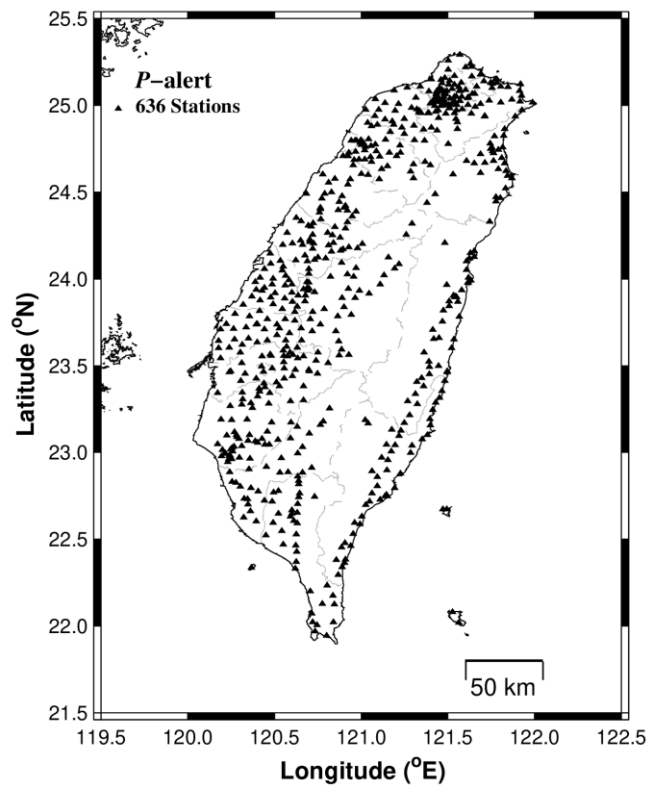


圖 20 palert 地震網測站分布圖



圖 21 地震事件震央分布圖

表 1 規模與波形統計

Event magnitude	2 - 3	3 - 4	4 - 5	5 - 6	6 - 7
Number of waveforms	9	427	668	555	138

1797 個波形圖中含 ENZ 三軸波形，而模型的輸入資料除了三軸波形圖還包含 STA、LTA、Characteristic Function 於三軸上的特徵，類神經網路模型的輸入特徵包含 ENZ 三軸波形總數為 12。而圖 22 為 P 波 SNR 分布圖，圖 23 為 S 波 SNR 分布圖。

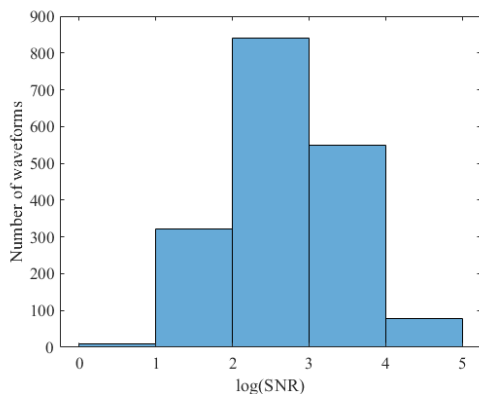


圖 22 P 波 SNR 分布圖

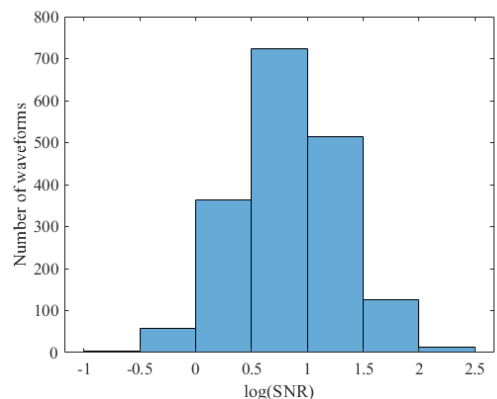


圖 23 S 波 SNR 分布圖

標記資料的部分分別為 P 波 S 波以及整個事件做標記，在 P 波發生的區間標記為 1，其餘為 0，以及 S 波發生區間為 1，其餘為 0，事件發生區間為 1，其餘為

0，如圖 24 所示。

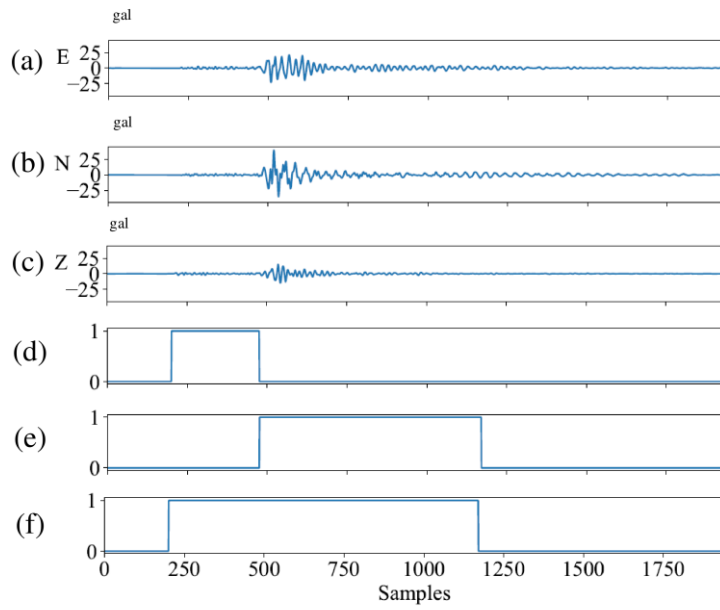


圖 24 資料標記範例

圖 24 中(a)、(b)、(c)為 ENZ 三軸波形資料，(d)為 P 波的標記資料，(e)為 S 波標記資料(f)為事件標記資料。

### 5.3 模型架構

本研究提出兩種模型分別如圖 25、26 所示。

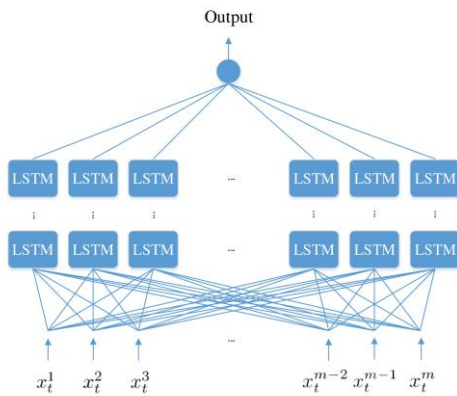


圖 25 Single Output Model

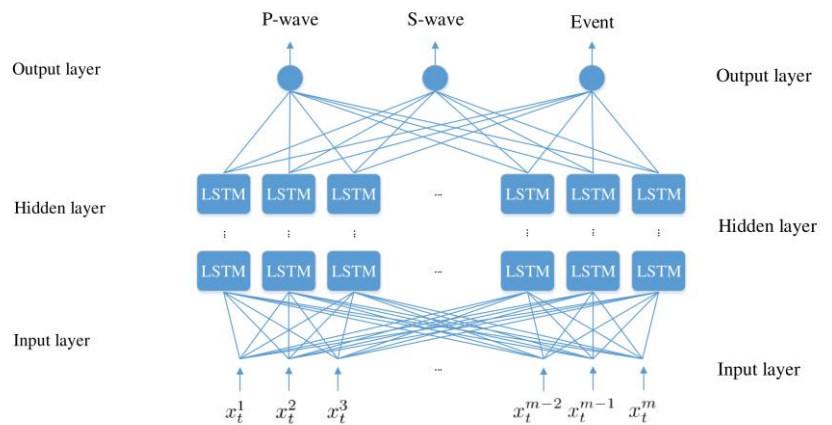


圖 26 Multi Output Model

圖 25 及 26 分別是 Single Output Model 及 Multi Output Model，兩者架構基本上一樣，差別在於輸出部分，Single Output Model 顧名思義只輸出一個值，可以是對 P 波、S 波、事件的機率，而 Multi Output Model 則是同時輸出 P 波、S 波、事件的機率，而圖中  $x$  代表輸入的特徵， $x$  上標數字代表第幾個輸入特徵，而研究中採用 12 個特徵，故  $m$  為 12，而  $t$  則為第  $t$  個時間點。

兩個模型架構中的 Hidden layer 皆由數層 LSTM 組成，最後再連接到全連接層，在 Single Output Model 中全連接層神經元數為 1，Multi Output Model 中為 3，接著通過 Sigmoid 函式得到機率輸出。LSTM 架構可參考章節 4.3，採用 LSTM 遞迴式神經網路可以於波型的每個時間點即時的輸出該時間點的 P 波、S 波、事件機率，如圖 27 所示，而模型於每一個時間點取 12 個特徵作為輸入，12 個特徵於章節 5.2 中提及。

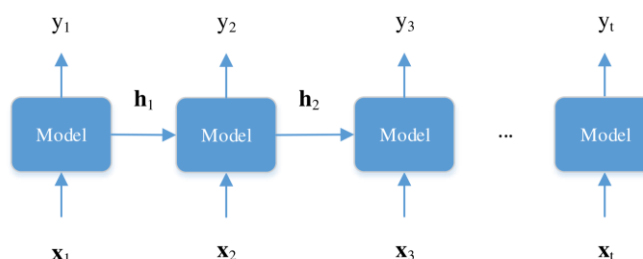


圖 27 模型於時間步展開示意圖

圖 27 中  $x$  為輸入特徵， $y$  為於該時間點輸出之機率，Model 的部分則為圖 25 及 26 所示，對於 Single Output Model 來說  $y$  是 P 波或 S 波或事件的機率，對 Multi Output Model 來說則包含三者的機率。

## 5.4 訓練過程

訓練中採用 Cross Entropy 為損失函式，目標為最小化損失函式計算出的損失值，而優化過程採 Adam 優化器，learning rate 為 0.003 訓練 150 輪。

## 5.5 實驗評估

以下實驗主要以評估 Precision、Recall、F score、False Positive Rate(FPR)為主。在介紹這些指標前先介紹四個名詞 True Positive(TP)、False Positive(FP)、True Negative(TN)、False Negative(FN)，TP 為模型預測為有地震實際也有地震的情況，FP 為將雜訊誤報為地震的情況，TN 為模型成功分辨雜訊為雜訊的情況，FN 則為模型將地震判斷為雜訊的情況。而  $TPR = TP / (TP + FN)$ ， $Recall = TP / (TP + FN)$ ， $F\ score = 2 * (Precision * Recall) / (Precision + Recall)$ ， $FPR = FP / (TN + FP)$ 。

在評估的過程中採用 3-fold cross validation，在每次實驗接隨機將資料集切成 3 等分並隨機選一等分為測試集，另外兩等分為訓練集，且每個實驗結果皆訓練 30 個模型取平均。第一個實驗評估了模型中 LSTM layer 的層數與神經元數量，結果如圖 28、29 所示。圖 28 中 layer 為 LSTM 層數，由實驗中可以看出層數 2 的 F score 得分最高，故接下來評估層數設置為 2。圖 29 中 n 為 LSTM 神經元數，實驗中 32 個神經元 F score 得分最高故之後實驗 LSTM 神經元皆設置為 32，圖 28 與圖 29 實驗皆採用 Single Output Model 用於偵測 P 波的模型。

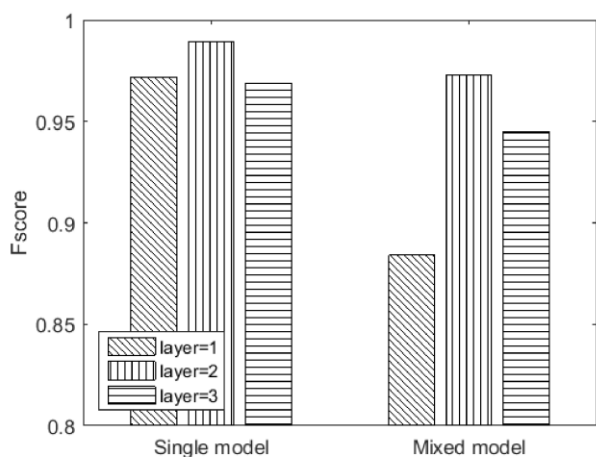


圖 28 LSTM 層數實驗結果

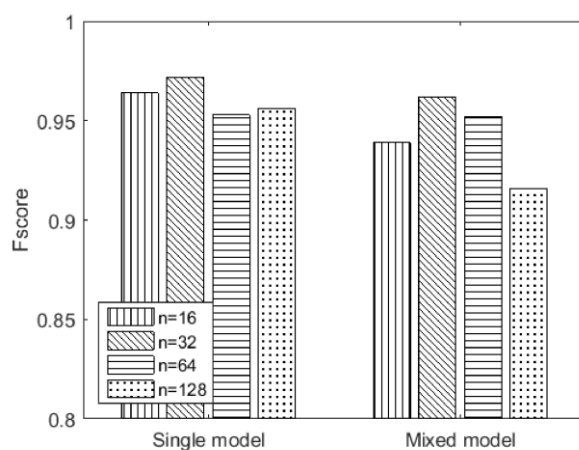


圖 29 LSTM 神經元數實驗

在模型給出個時間點的 P 波、S 波、事件機率後，為了判定事件是否發生以及何時發生而提出了 2 個參數分別是  $\eta_t$ 、 $\eta_p$ ，判定方法為當模型於某時間點輸出機率高於  $\eta_p$ ，且接續  $\eta_t$  個點也大於  $\eta_p$ ，滿足此條件變判斷該點為地震發生點，而圖 30 則針對這  $\eta_t$ 、 $\eta_p$  做評估。圖 30 中 ROC 曲線評估了 Single Output Model 用於偵測 P 波時  $\eta_t$ 、 $\eta_p$  對 FPR 及 TPR(Recall) 的影響，圖中不同顏色的線代表有不同的  $\eta_t$ ，線上不同的點代表著不同的  $\eta_p$ 。當  $\eta_p$  上升 FPR 下降 TPR 下降，因判定條件變嚴格故 FPR、TPR 下降，代表低誤報但同時更容易忽略地震事件。反之  $\eta_p$  下降，TPR 及 FPR 上升，因判定條件變寬鬆故 TPR、FPR 上升，代表更容易誤報但同時也能偵

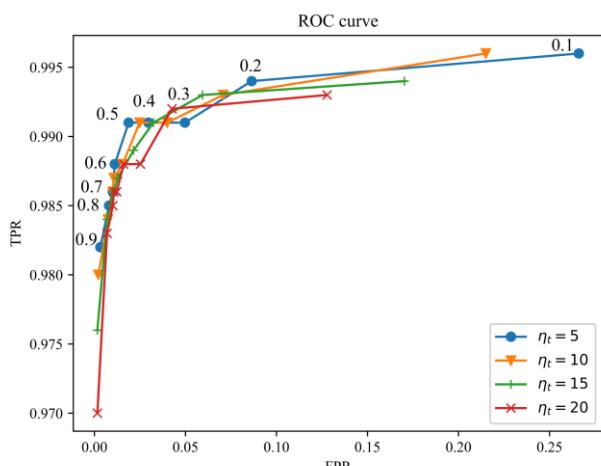


圖 30 ROC 曲線

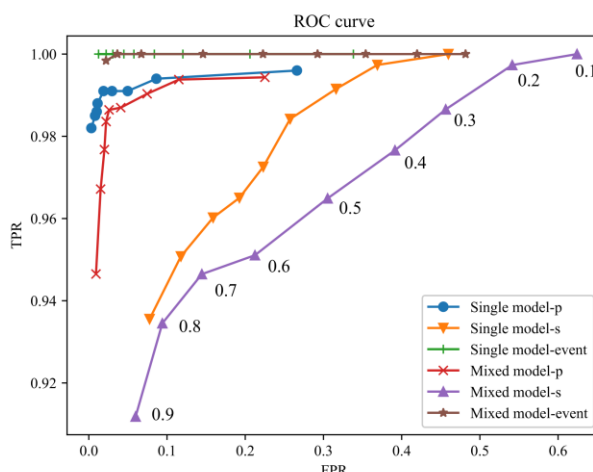


圖 31 不同模型的 ROC 曲線

測出更多地震事件。而 $\eta_t$ 表現與 $\eta_p$ 相似，當 $\eta_t$ 上升 FPR、TPR 下降，反之，TPR 及 FPR 上升。

接著評估 $\eta_p$ 對 Single Output Model 及 Multi Output Model 的影響，因 $\eta_t$ 對結果影響較小，故僅評估 $\eta_p$ ，並將 $\eta_t$ 設為 5，結果如圖 31 所示。圖 31 中展示了各模型對於 P 波、S 波及事件在 $\eta_p$ 影響下的結果，其中可以看出 Single Output Model 在 P 波與 S 波偵測上都優於 Multi Output Model，因為 Multi Output Model 在同樣的隱藏層參數下須學習同時偵測 P 波、S 波及事件故表現不及僅學習偵測 P 波或 S 波或事件的 Single Output Model。

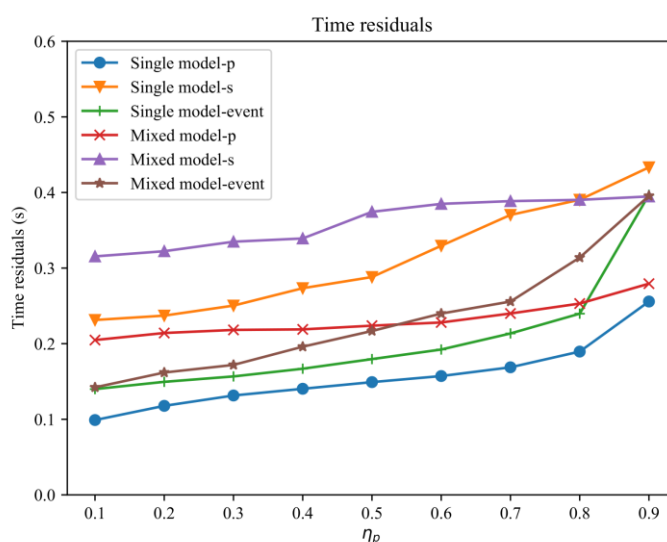


圖 32 不同模型的 Time Residual

接著評估了 Time Residual，Time Residual 是指模型判定 P 波、S 波、事件的發生點與實際發生點的時間差，以下實驗取各測試資料的 Time Residual 平均。圖 32 顯示了各模型的 Time Residual 在 $\eta_p$ 影響下的結果，可以看出 $\eta_p$ 越高代表偵測條件越嚴格造成 Time Residual 上升，而 $\eta_t$ 較不影響結果故設為 5，而 Single Output Model 在偵測 P 波達到 0.25 秒以下的 Time Residual，在偵測 S 波達到 0.45 秒以下的 Time Residual，在偵測事件達到 0.35 秒以下的 Time Residual，而 Multi Output Model 在 P 波、S 波、事件偵測上的 Time Residual 都較 Single Output Model 來的高，原因如先前所提。比較 Single Output Model 與傳統的 criterion-based picker 在 P 波偵測上的表現，criterion-based picker 中會依據 STA/LTA 的比值來判斷地震事件的發生，當比值高於一預先訂定的閾值  $\delta$  便判定地震事件發生，而為了公平的比較兩方法的效果，便實驗了  $\delta$  對方法的影響。



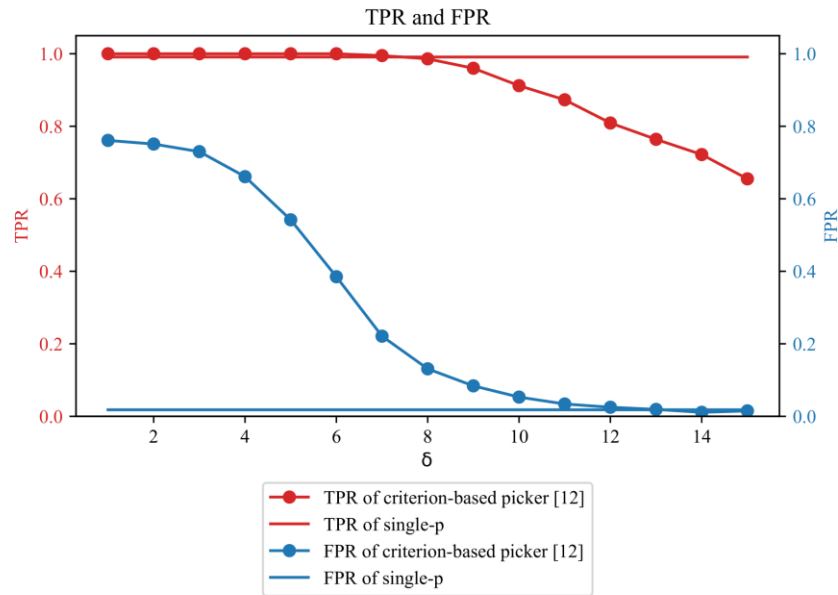


圖 33  $\delta$  對於方法的影響

圖 33 中可以看到  $\delta$  對於 Single Output Model(single-p)沒有影響，因方法中沒使用到該參數，而對 criterion-based picker 是有影響的，而在  $\delta=8$  時 criterion-based picker 的 TPR=0.986，FPR=0.131，相較其他值比起來是比較好的結果，故採此結果與 Single Output Model 做比較，結果如表 2 所示。

表 2 criterion-based picker 與 Single Output Model 比較

	TPR	FPR	Time residuals	Alarm time
Single model-p	0.991	0.018	0.149(s)	0.289(s)
Criterion-based	0.986	0.131	0.195(s)	2.194(s)

表 2 中 Single Output Model(Single model-p)  $\eta_p=0.5, \eta_t=5$ ，可以看到在 TPR、FPR、Time Residual、Alarm time 上表現都比 criterion-based picker 好，表示 Single Output Model 可以在較短的時間(Alarm time)發出準確的警報，而傳統的 criterion-based picker 需要於 STA/LTA 比值高於閾值後取 2 秒波形再進行後續判斷，故會需要較久的 Alarm time，且在 FPR 上也較高代表較容易受到雜訊影響。

## 5.6 具體結果

首先我們拿了 2018 花蓮地震中 palert 測站 W21 所收到的波形做偵測，結果如圖 34 所示。圖 34 中(a)、(b)、(c)分別是 ENZ 三軸波形，(d)、(e)、(f)分別是模型對 P 波、S 波、事件的輸出結果。我們試著將模型與 Earthworm 串接，而模型實作使用 python 與 tensorflow，而與 Earthworm 的串接則透過 PyEW 套件實現，現在該套件於 linux 及 windows 上皆可運行。在串接上後便可以透過 Earthworm 與其他模組串接，而我們有成功與 tankplayer 串接，透過 Earthworm 讀取 tankplayer 播放的歷史波形並將偵測結果傳至 tcpd 進行後續定位發布功能。

圖 35 為與 Earthworm 串接範例，該範例中採用台灣時間 2014/12/31 11:05 之地震事件，其中 4 個測站的偵測結果，圖中紅線表示模型判定 P 波到來的點，紫線表示實際 P 波到來的點。

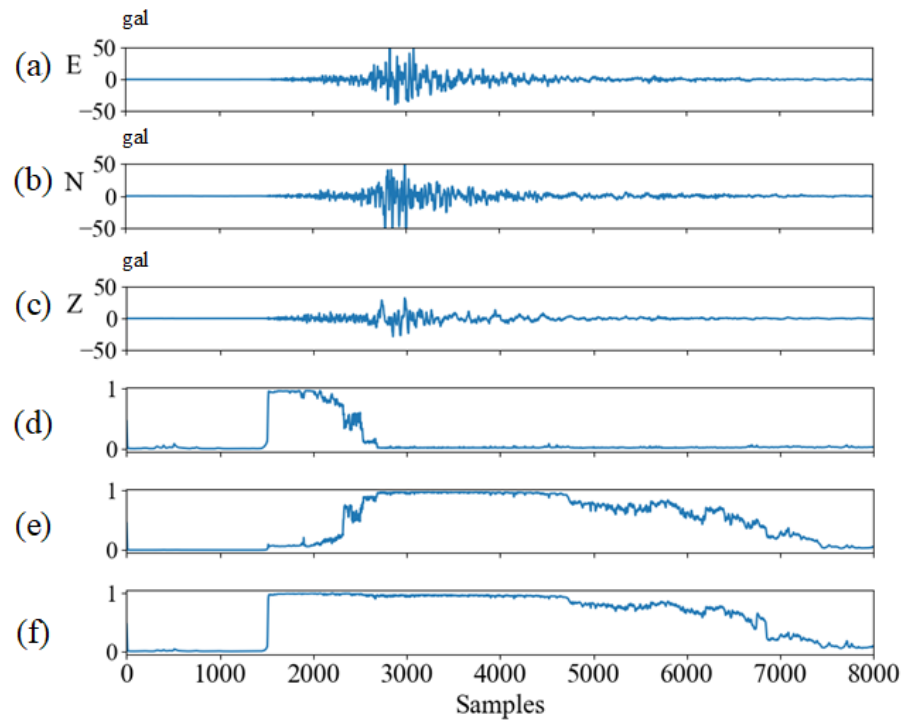


圖 34 花蓮地震範例

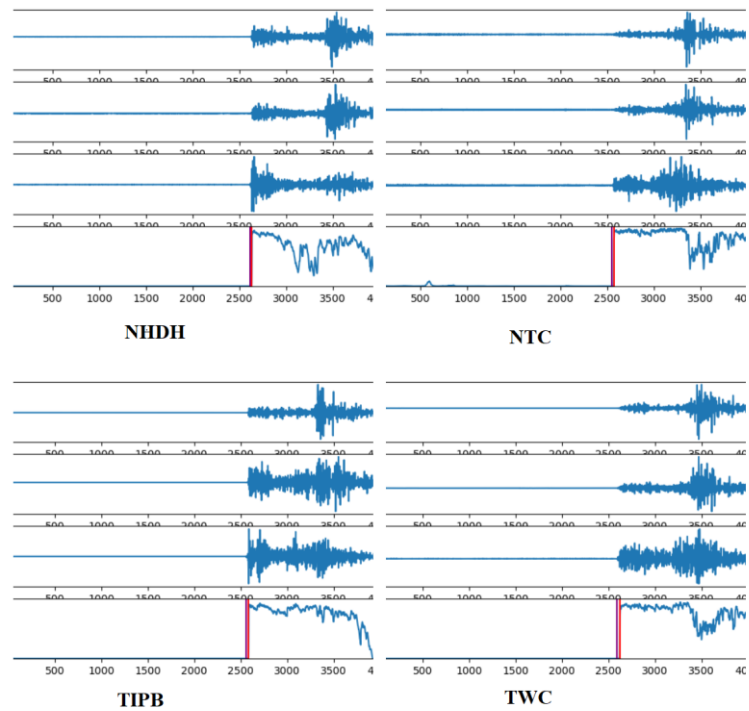


圖 35 Earthworm 串接範例

## 5.7 結論

本研究主要提出利用遞迴神經網路即時偵測 P 波、S 波及事件的發生，在評估過程中針對各種因素做評估，結果顯示提出的方法有著不錯的表現，能準確的偵測地震並迴避雜訊影響，且也能準確的判定發生時間，也將提出的方法與 Earthworm 串接，盼將來可以應用到即時系統上於預警中提供準確的偵測結果。

## 6 深度卷積網路於 P 波 S 波檢測之應用

### 6.1 簡介

本研究主要在於將深度卷積網路應用於 P 波 S 波檢測，現在地震紀錄中的 P 波、S 波到時皆是人工檢測的結果，而本研究主要想將該過程交由深度卷積網路處理，盼能減少人力的消耗，並有準確的結果。

### 6.2 資料處理

資料集從 2016~2017 取了 4028 張包含 ENZ 三軸之波形圖，其中隨機選 3000 張用於訓練 1028 張用於測試，並對波形 normalize 將 ENZ 三軸除以三軸中最大值，且每張波形皆為 30 秒長，以此剪去震度對結果的影響，而訓練資料的 SNR 分布如圖 36、37 所示。標記資料的部分與章節 5.2 相同，範例可參考圖 24 所示。

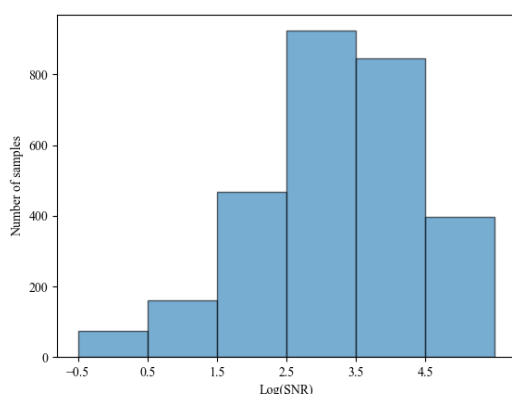


圖 36 訓練資料 P 波 SN

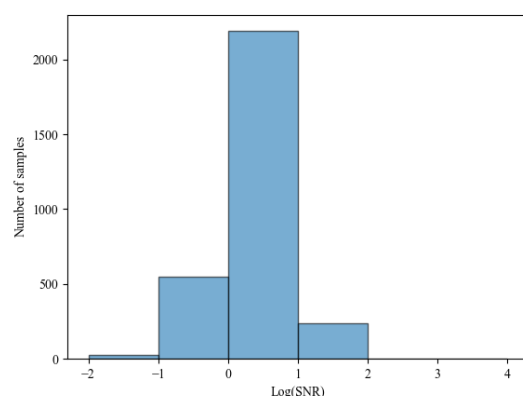


圖 37 訓練資料 S 波 SNR 分布

### 6.3 模型架構

網路架構如圖 38 所示，模型主要由 4 個區塊組成，分別是 ResNet50、Multi Grid、ASPP、Conv&Upsample，模型的輸入是三軸波形，輸出是 2 個 30 秒長的向量，值介於 0 到 1 之間，一個向量代表 P 波的機率，一個代表 S 波機率。模型的各區塊介紹如下。

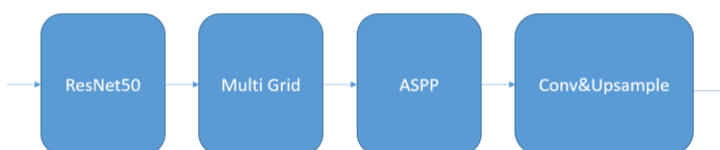


圖 38 深度卷積網路架構

### 6.3.1 ResNet50

Residual Net(ResNet)最一開始提出是被用於影像分類任務，而後來也常被用於其他任務中，例如影像切割、GAN 網路、Few Shots Learning，在這些任務中 ResNet 常扮演著特徵抽取的腳色，而在本研究中 ResNet 也扮演著同樣的腳色，對輸入的波形圖進行特徵學習，透過這些特徵找出 P 波、S 波的位置。而 ResNet50 代表深度 50 層的網路，基本是由多層卷積組成，大致架構如圖 39 所示。

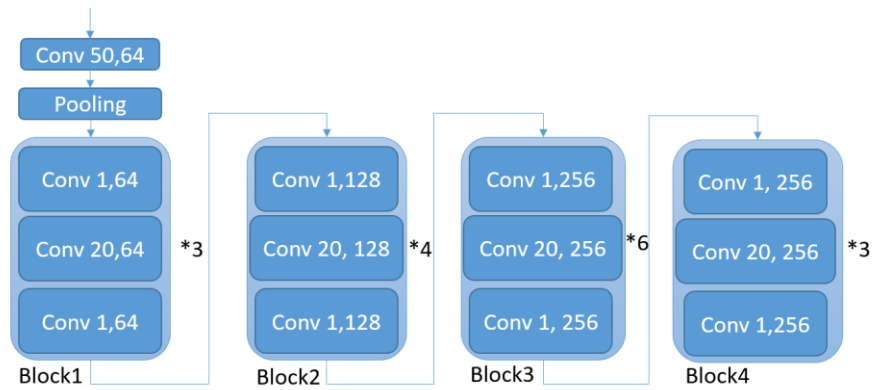


圖 38 ResNet50

圖 38 中描繪了經稍微修改後的 ResNet50 架構，在模型的最一開始是一層 kernel size 為 50 的 1 維卷積有著 64 個 filter，stride 為 2，接著經過一層 maximum pooling，stride 為 2，至此整個波形圖長度已縮小 4 倍，接著是 Block1，Block1 中包含 3 個重複的單元，而一個單元包含 3 個卷積，分別是 kernel size 為 1,64 個 filter 的 1 維卷積、kernel size 維 20,64 維的 1 維卷積、kernel size 為 1,64 個 filter 的 1 維卷積，接著的其他 Block 基本上與 Block1 組成大致相同，差別是單元重複次數與 filter 數量不同，個 Block1、2 的最後一個單元中的最後一個卷積 stride 為 2，故在該 Block 的輸出皆是輸入的 1/2。透過這些卷積後，模型便能根據波形學出 P 波 S 波特徵，接著輸出給下一層做更進一步處理。

### 6.4 Multi Grid

Multi Grid 層主要是將原先的 ResNet 加深，通常加深網路認為會有更好的表現，並且增加了模型的視野，因每個 Block 會經 stride 故令下一個 Block 會有更大的視野，若只是單純的複製 ResNet 最後一個 Block 並將該 Block 中最後一個單元的最後一個卷積 stride 改為 2，此舉雖然會增加後續 Block 的視野，但經過多次縮小會令最終的特徵向量解析度太低，不利於後續判斷 P 波、S 波詳細位置。故為

了要同時兼具大視野又不把特徵圖縮小，在 Multi Grid 中採用了空洞卷積，空洞卷積主要是在原先卷積中跳過  $n$  格，以此來獲得更大的視野且也不會輸出的縮小特徵圖，而  $n$  又稱為空洞率，而 Multi Grid 複製了 3 份 ResNet 最後一個 Block 並將其中 kernel size 非 1 的卷積改為空洞卷積，3 份複製出的 Block 的空洞卷積各自有著不同的空洞率，目前分別設為 1,2,4，Multi Grid 架構如圖 40 所示。

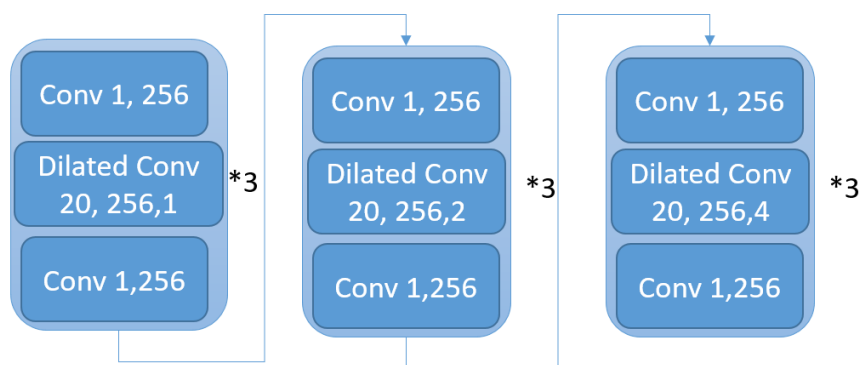
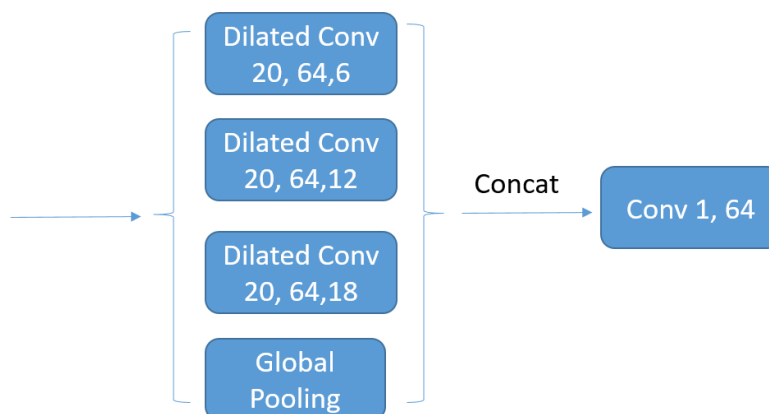


圖 40 Multi Grid

### 6.4.1 ASPP

Atrous Spatial Pyramid Pooling (ASPP)層主要用於針對多尺度目標進行學習，多尺度目標意指學習目標大小會有不同，在這裡指 P 波特徵與 S 波特徵可能長度會不一樣，因每張波形圖 P 波與 S 波的時間差不一樣，故利用此層進行多尺度捕捉。而做法是採用空洞卷積以不同空洞率進行捕捉，不同空洞率的空洞卷積有著不同的視野大小，故可以捕捉不同尺度的目標，以及配合上一個全局池化層，最後將所有特徵串接後經過一個 kernel size 為 1 的卷積輸出，而架構如圖 41 所示。



#### 圖 41 ASPP

圖 41 中 ASPP 有 3 個空洞卷積各自空洞率為 6,12,18，且 filter 皆為 64 個，再加上 1 個全局池化，這幾個空洞卷積與全局池化各自獨立運行，最後將輸出以 filter 維度串接後經 1 個 kernel size 為 1 filter 為 64 的卷積後輸出。

## 6.4.2 Conv&Upsample

最後這層主要是將由 ASPP 輸出的低解析度特徵圖上採樣至原本輸入的 30 秒長度，主要是以轉至卷積方式實現，經轉至卷積後得到 30 秒長度的特徵圖，再透過 1 個 kernel size 為 1 filter 為 2 的卷積將 filter 數量降至 2，2 個 30 秒特徵圖經過 sigmoid 後輸出對應至 P 波 S 波於 30 秒間可能出現的機率，架構如圖 42

所示。



圖 42 Conv&Upsample

如圖 42 所示，將輸出經 16 倍上採樣後還原至 30 秒長度，並透過 1 個卷積輸出 P 波 S 波機率。

## 6.5 訓練過程

訓練過程採 Cross Entropy 做損失函式，優化器為 Adam，訓練 1000 次，採變動式學習率，學習率會隨著訓練次數下降，學習率如下式所示，其中  $n$  為總訓練次數， $i$  為第幾輪訓練， $lr$  為該輪學習率， $lr0$  為初始學習率，次處設為 0.0001。

$$lr = (1 - (i/n))^{0.9} * lr0$$

## 6.6 具體結果

用於評估結果的測試資料含 1028 張波形圖，其 SNR 分部如圖 43、44 所示。

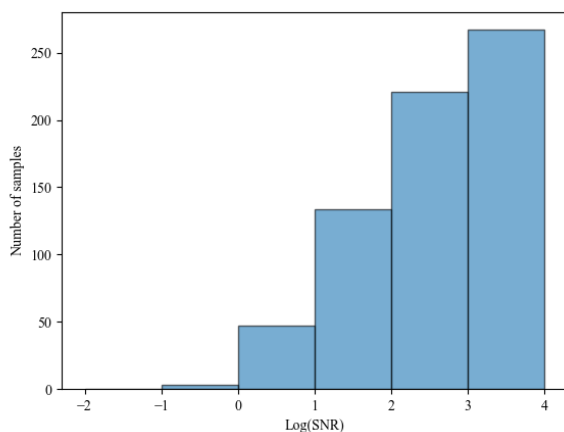


圖 43 測試資料 P 波 SNR 分部

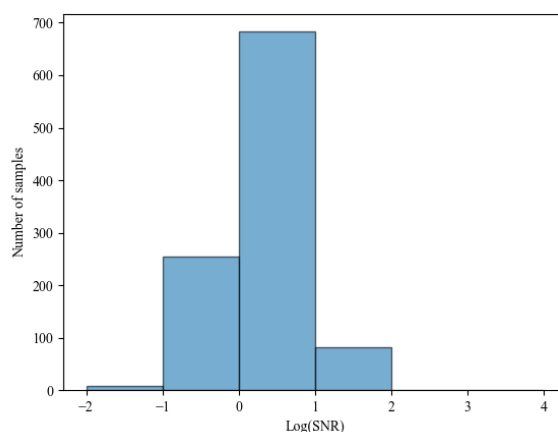


圖 44 測試資料 S 波 SNR 分部



評估的方法與章節 5 類似，採用  $\eta_t$ 、 $\eta_p$  方式評估 Time Residual。當模型輸出機率大於  $\eta_p$ ，且連續  $\eta_t$  個點皆大於  $\eta_p$ ，便判定該點為事件發生點，而 Time Residual 為實際事件發生點與模型判定點的差。因本研究中沒有加入雜訊資料，故僅先評估 Time Residual，結果如圖 45、46 所示。圖 45、46 評估了  $\eta_t$ 、 $\eta_p$  對 Time Residual 的影響，圖中各點為測試資料於該條件下的平均 Time Residual，可以看到當  $\eta_p$  上升，篩選條件越嚴格時 Time Residual 下降，因嚴格的篩選條件可以避免再事件來臨前的雜訊干擾，而  $\eta_t$  上升也有類似效果，提升篩選條件另 Time Residual 下降。

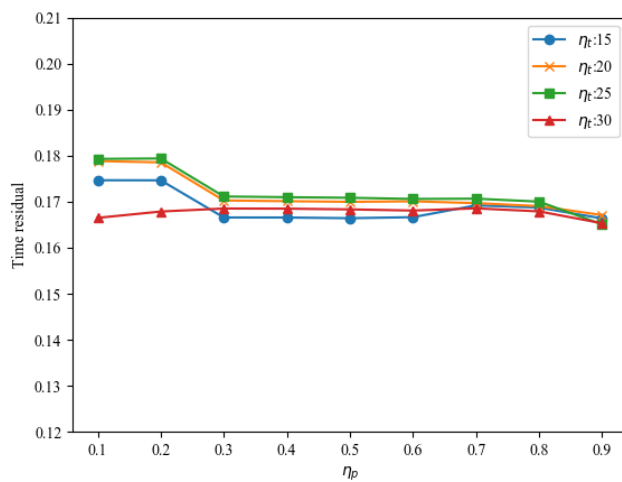


圖 45 P 波 Time Residual

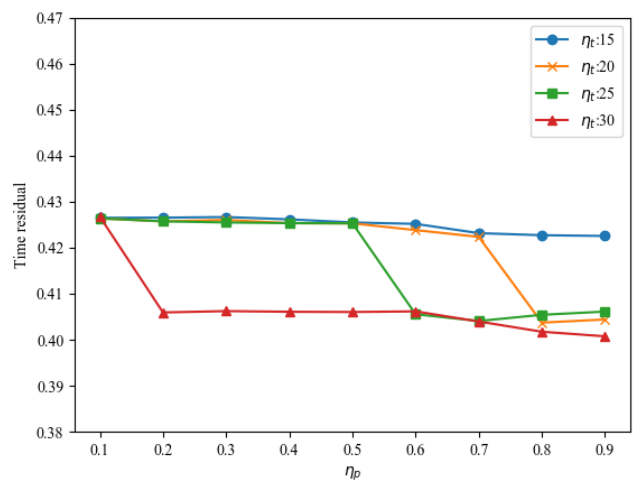


圖 46 S 波 Time Residual

圖 47、48 為模型輸出範例，其中 (a)、(b)、(c) 為以除以最大值的三軸波形，(d)、(e) 分別為 P 波及 S 波標記，(f)、(g) 則是模型輸出的 P 波、S 波機率，在這兩個例子中模型給出的機率很高，且其輸出形狀與標記相似度高。

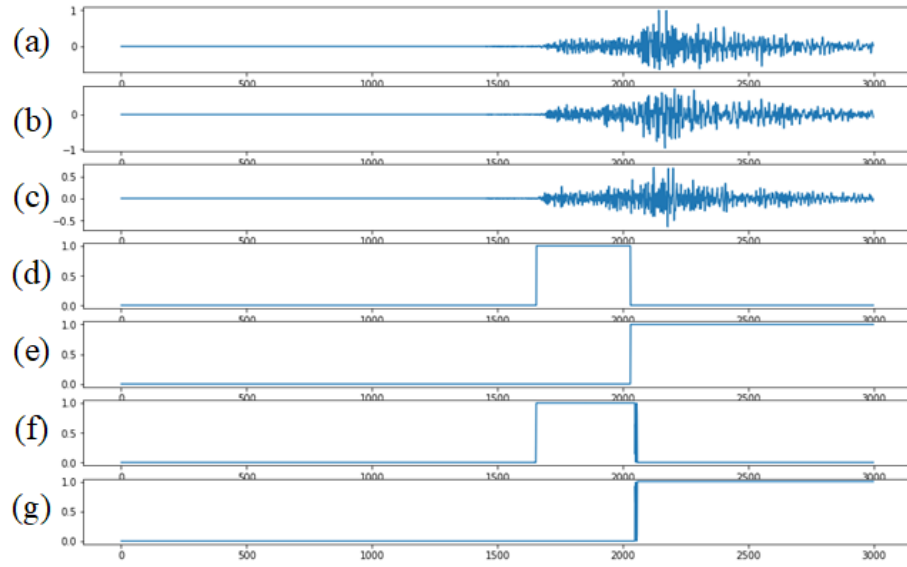


圖 47 模型輸出範例(1)

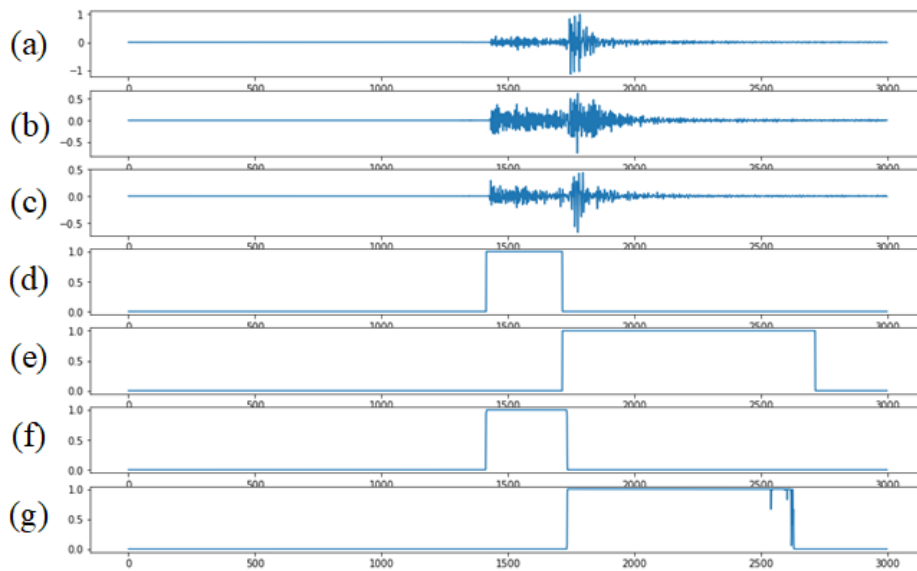


圖 48 模型輸出範例(2)

## 6.7 結論

該研究在現階段有了初步的成果，如上所示，可以看到模型可以分辨波形中 P 波、S 波所在的位置，但仍有些 Time Residual，不過相信之後使用更豐富的資料集後應該可以壓低 Time Residual，進而達到更好的表現，盼未來可以實際應用在現實狀況中，以降低繁複的人工處理。